ALMA MATER STUDIORUM
UNIVERSITÀ DI BOLOGNA

School of Science
Department of Physics and Astronomy
Master Degree Programme in Astrophysics and Cosmology

The Search for Vulcanoids: A Comprehensive Analysis

Master's Thesis

Supervisor:
Prof. Gabriele Umbriaco

Co-supervisors:
Dr. Albino Carbognani
Dr. Silvia Galleti

Presented by:
Thimea Armenio

Session I - July 2026
Academic Year 2025-2026

Abstract

Our understanding of the architecture of the Solar System has grown significantly in recent decades. The discovery and characterisation of various asteroid populations have provided fundamental insights into the nature and origins of minor bodies. However, among the few stable dynamical niches that remain largely unexplored today is the region interior to Mercury's orbit, where the Vulcanoid Asteroids are hypothesised to reside. This Master's Thesis presents a comprehensive analysis of the Vulcanoid Zone, combining theoretical dynamical models with future observational strategies. The orbital boundaries and the extreme thermal and collisional environment of this intra-Mercurial region are investigated, highlighting how continuous collisional grinding and non-gravitational forces heavily constrain the survival of primordial material. Despite these critical conditions, the existence of kilometer-scale fragments cannot be definitively ruled out on theoretical grounds alone.

To address the historical challenges of observing objects in such close proximity to the Sun, this thesis conducts a detailed signal-to-noise ratio (SNR) analysis and, based on these constraints, a specific observational campaign tailored for the upcoming total solar eclipse on August 2, 2027, is proposed. By outlining the required optical systems and detection strategies, this work provides a concrete pathway for either discovering these elusive objects or placing rigorous limits on their population, thereby advancing our understanding of the early formation of the inner Solar System. The principal original contributions of this thesis include the development of an eclipse-specific signal-to-noise model, the construction of a Vulcanoid detectability map combining all major observational limits, and the design of dedicated observing campaigns for the 2026 and 2027 total solar eclipses.

Contents

List of Figures

List of Tables

Chapter 1

Introduction

Our Solar System formed approximately 4.6×10^9 years ago [10]. In its present-day configuration, beyond the eight planets, the Solar System is populated by millions of minor bodies, including asteroids, comets, meteoroids, Trans-Neptunian Objects (TNOs), and centaurs. They are typically classified by their heliocentric orbits and/or physical characteristics, and undergo distinct evolutionary processes.

These rocky and icy bodies are distributed across various regions. Some follow highly eccentric paths, such as Near-Earth Asteroids (NEAs), while others reside in the outermost region known as the Kuiper Belt with orbits between 30 and 55 AU [19]. The dwarf planet Pluto is one of the largest known members of this region and the first Kuiper Belt Object (KBO) to be discovered. The oldest and best-known population is the Main Asteroid Belt, a region located between 2 AU and 3.4 AU [1] [28] from the Sun, between the orbits of Mars and Jupiter. It accounts for the highest concentration of asteroids, more than 90% of the known asteroids have already been discovered. These objects have diameters ranging from a few hundred meters to hundreds of kilometers. Their physical properties are equally varied, spanning from porous, rubble-pile structures to solid metallic or silicate compositions. Due to their intrinsically low luminosity, asteroids generally require telescopic observation for detection and characterisation.

A key property of these bodies is their rotational motion, which induces periodic variations in their observed light curves. For most asteroids observed photometrically, the periodic brightness variations induced by rotation generally exhibit amplitudes smaller than about one magnitude, and the distribution of rotation periods derived from light curve analysis ranges from a few hours up to a few tens of hours, with the majority of measured values falling between approximately 3 and 18 hours [2] [56] [1].

While the outer and central regions of the Solar System have been extensively mapped, its innermost region, strictly confined within the orbit of Mercury, remains largely unexplored. In this extreme environment, dynamical models theorise the existence of an elusive and yet-undiscovered population of asteroids on stable intra-Mercurial orbits, known as Vulcanoids. Understanding this population is important because Vulcanoids may represent an extreme inner-Solar-System analogue of primordial planetesimal reservoirs. The search for and characterisation of this hypothetical class of asteroids is therefore the primary focus of this work.

[1] AU is the Astronomical Unit, which corresponds to the distance Earth-Sun. $1\ \text{AU} \approx 149,600,000\,\text{km}$ [19].

[2] These ranges are derived from statistical analysis and should be interpreted as representative of the observed asteroid population rather than as strict physical limits.

1.1 Physical Properties of Asteroids

When a new asteroid is discovered, the primary information that can be determined from the initial observations is its orbit [3], which allows the object to be dynamically classified within the Solar System and enables predictions of its future motion.

Although orbital parameters are essential for describing the dynamical behaviour of an asteroid, they do not provide direct information about its physical properties [58] [46], such as its size, shape, rotation, or surface composition. These characteristics are fundamental for understanding the nature, origin, and evolution of asteroid populations. Indeed, these physical and dynamical properties become particularly relevant in the Vulcanoid region, where thermal and radiative effects are greatly enhanced.

Photometric observations are among the most effective and accessible techniques for deriving these quantities, particularly for faint or recently discovered objects for which spectroscopic data are often unavailable. Time-series photometry allows for the determination of an asteroid's rotational period through the investigation of periodic brightness variations induced by its rotation. These variations arise primarily from the irregular shape of the object and, to a lesser extent, from heterogeneities in surface albedo. Therefore, light curve analysis provides insight into the asteroid's rotational state and constraints on its shape elongation.

In addition to rotational properties, photometric measurements can be used to estimate the asteroid's size using the following relation [31] [47]:

$$D = \frac{1329}{\sqrt{p_V}} \cdot 10^{-H/5} \tag{1.1}$$

where H is the absolute magnitude, i.e., the apparent magnitude the asteroid would have if it were located 1 AU from both the Sun and the Earth, at a phase angle of zero [4], while p_V is the visual geometric albedo.

The geometric albedo p_V is defined as the ratio of the object's visual brightness at zero phase angle to that of a Lambertian disc, which reflects all incident light and scatters it equally in all directions, with the same cross-section. However, to fully characterise the energy balance and the reflective properties of an asteroid, it is often necessary to consider the Bond albedo (A_B), which represents the fraction of total incident solar radiation reflected by an asteroids and all other bodies of the Solar System, in all directions. These two quantities are related by the following expression [45]:

$$A_B = p_V \cdot q \tag{1.2}$$

where q is the phase integral, a parameter that accounts for the scattering properties of the surface across all phase angles.

Since the geometric albedo p_V is a strictly intrinsic parameter related to surface mineralogy, its estimation represents the primary source of uncertainty in diameter calculations. This uncertainty can be derived through the propagation of errors in absolute magnitude H and albedo, according to the following equation:

[3] The determination of a reliable orbit requires an observational arc of sufficient length and quality; orbits derived from very short arcs are often affected by large uncertainties and may be significantly revised as additional observations become available.

[4] Usually denoted as α, this is the Sun-object-Earth angle.

$$\sigma_D = D\sqrt{\left(\sigma_H \frac{\ln 10}{5}\right)^2 + \left(\frac{\sigma_{p_V}}{2p_V}\right)^2} \tag{1.3}$$

where D and σ_D are the estimated diameters of the asteroid and its associated uncertainties, σ_H is the uncertainty on the absolute magnitude H, while p_V is the geometrical visual albedo and σ_{p_V} its uncertainty.

In the absence of direct measurements, such as thermal infrared observations, p_V is typically estimated from the asteroid's classification. This emphasises the fundamental link between an object's physical dimensions and its surface composition, which is categorised through taxonomic classification.

1.1.1 Taxonomic Classes and Classification of Asteroids

Asteroids can be classified based on their spectral and photometric properties into taxonomic classes. This classification provides a framework for inferring an object's composition and expected albedo. The following table summarises the typical average visual geometric albedo [85] for the main taxonomic complexes:

Taxonomic Complex	Average Visual Albedo	Surface Nature
S (Silicaceous)	0.208 ± 0.079	Stony, olivine/pyroxene-rich
C (Carbonaceous)	0.071 ± 0.040	Primitive, organic-rich, dark
X (Complex)	0.098 ± 0.081	Metallic or enstatite-rich
D (Dark)	0.086 ± 0.053	Very dark, carbon-rich
V (Vesta-like)	0.297 ± 0.131	Basaltic, highly reflective

Table 1.1: Typical average visual geometric albedo values for the main asteroid taxonomic classes.

Asteroids consist of rocks and regolith that reflect sunlight; their reflectance spectra can be measured from Earth-based observations, which reveal broad absorption features indicative of the elements and minerals present on their surfaces. In particular, diagnostic absorption bands are mainly associated with silicate minerals, metals, and hydrated phases [24]. Thus, the shape of the continuum and the presence, depth, and position of absorption features are used to divide asteroids into different taxonomic classes. It should be noted that asteroids can be made up of mixtures of materials in varying proportions and can exhibit surface alteration processes such as space weathering; for this reason, spectroscopic analysis alone often provides non-unique information on composition.

The most widely used classification is the Tholen Taxonomy, developed by Tholen (1984) [83] based on the earlier work of Chapman et al. (1975) [23]. This taxonomy is based on reflectance photometry obtained from the Eight-Colour Asteroid Survey (ECAS), covering a wavelength range from 0.31 to 1.06 μm, combined with geometric albedo measurements [94]. The Tholen system defines 14 primary taxonomic classes, each designated by a single letter. When an asteroid exhibits spectral characteristics intermediate between two classes, a two-letter designation is used [83]. The major classes in this taxonomy are the C, S, and X complexes, which together account for the majority of known asteroids.

- C-type asteroids are carbonaceous objects characterized by low albedos and generally featureless visible spectra, sometimes displaying a weak absorption feature near $0.7\,\mu m$ associated with hydrated minerals [83] [94]. These asteroids are considered compositionally primitive and are prevalent in the outer main belt, though a significant fraction of NEAs also belong to this class.
- S-type asteroids exhibit moderate albedos and spectra with prominent absorption bands near 1 and $2\,\mu m$, indicative of silicate minerals such as olivine and pyroxene, and are interpreted as rocky bodies [23] [83]. This class is particularly common among NEAs.
- X-type asteroids form a spectrally degenerate group characterized by relatively featureless spectra that span a wide range of albedos. In the Tholen taxonomy, this class is subdivided into E-, M-, and P-types on the basis of albedo, which are commonly associated with enstatite-rich, metallic, and primitive compositions, respectively [83].

The characteristic reflectance behaviour of the main taxonomic complexes in the visible wavelength range is illustrated in Figure 1.1 [20]. Most reflectance curves slope slightly differently between 450 and 750 nm, except for the C-complex, which has a substantially flat curve. The V, S, and D reflectance curves rise to varying degrees between 750 and 900 nm, while the X and T curves slope more gently or remain nearly stationary. This distinct reflectance pattern allows recognition of the taxonomic class, provided that infrared magnitudes are also used, which can significantly contribute to discriminating between the different curves [20].

Subsequent taxonomic schemes, including the Bus taxonomy and its extension, the Bus–DeMeo taxonomy, expanded upon the Tholen system by using higher-resolution visible and near-infrared spectra and refining class boundaries [14] [30].

1.2 Non-gravitational Effects in Asteroid Dynamics

The motions of celestial bodies are usually considered to be governed by the sole gravitational influence of the Sun and the major planets, but they are also affected by non-gravitational forces.

In addition to collisions, persistent non-gravitational effects can gradually alter their trajectories and rotational states. These forces arise from the interaction between solar radiation and the asteroid's surface. As discussed in the previous sections, an asteroid's response to sunlight depends on its physical characteristics, such as its size (D), albedo (p_V), and the composition of its regolith. The thermal re-emission of absorbed solar energy creates a small net thrust that, although minute, acts continuously, leading to measurable changes in the semi-major axis and spin rate. Understanding these effects is of fundamental importance for mapping the transport of asteroids from the Main Belt to the inner Solar System [60] and for accurately predicting the impact risk of potentially hazardous objects.

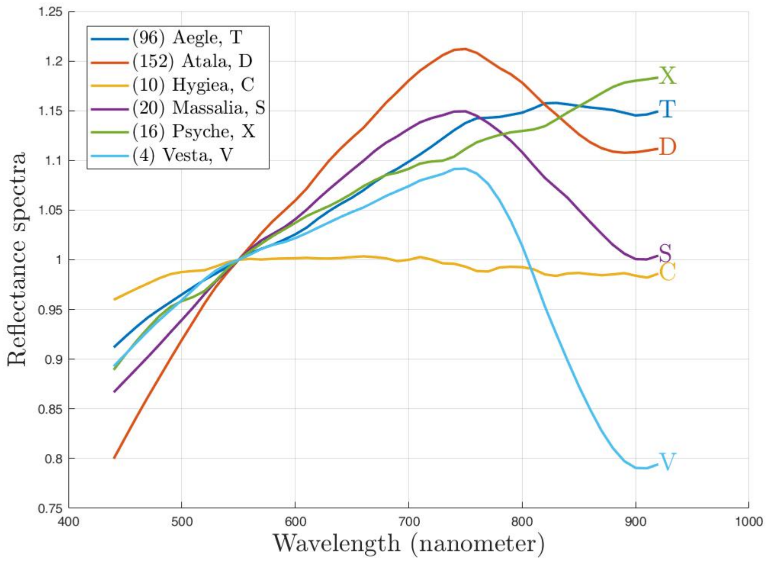

Figure 1.1: Representative visible reflectance spectra from the Small Main Belt Asteroid Spectroscopic Survey (SMASS II) for the main asteroid complexes. All spectra are normalized to unity at 550 nm. While the spectral slopes between 450 and 750 nm are broadly similar (with the notable exception of the C-complex), the complexes become more clearly differentiated toward the near-infrared. This enhanced separation facilitates asteroid taxonomic classification when photometric measurements extend into this wavelength range.

1.2.1 The Yarkovsky Effect

Ivan Osipovich Yarkovsky (1844–1902), a civil engineer who worked on scientific problems in his spare time, first proposed the effect that now bears his name. Yarkovsky noted that the diurnal heating of a rotating object in space would cause it to experience a force that, while tiny, could lead to large secular effects in the orbits of small bodies, especially meteoroids and small asteroids [66].

Description of Diurnal Component

The fundamental mechanism behind Yarkovsky's diurnal effect is illustrated in Figure 1.2a, which shows a spherical meteoroid in a circular orbit about the Sun. For simplicity, the meteoroid's spin axis is taken to be normal to the orbital plane, so that the Sun always stands on its equator. Insolation heats up the sunward side, and this thermal energy is reradiated into space, typically in the infrared part of the spectrum, unless the meteoroid is very close to the Sun.

As the asteroid rotates, it absorbs solar radiation. Due to thermal inertia, the afternoon hemisphere reaches higher temperatures than the morning hemisphere. When this warmer region emits infrared photons, they carry away momentum according to the relativistic relation $p = E/c$ where p is the photon's momentum, E its energy, and c the speed of light. Since more energy and momentum are radiated from the hotter part of the meteoroid than from the colder side, the body experiences a net recoil force (or kick) in the direction opposite to the emission to maintain the conservation of momentum.

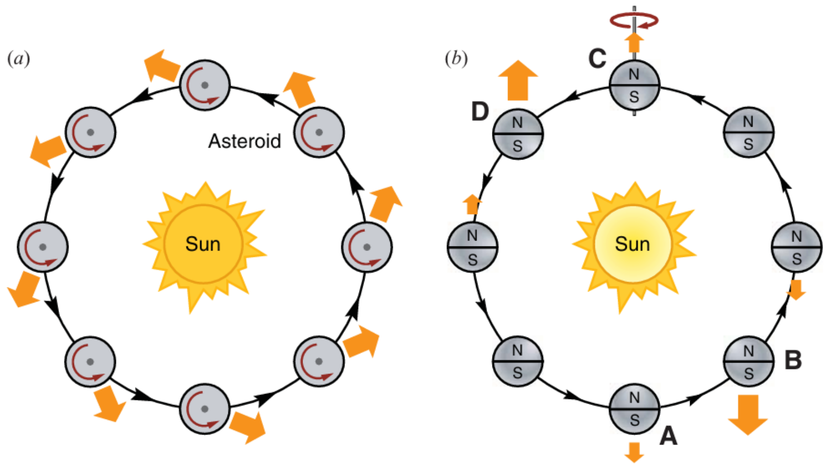

Figure 1.2: Schematic illustration of the Yarkovsky effect. (a) Diurnal component: the asteroid's spin axis is perpendicular to the orbital plane. Absorbed solar radiation is re-emitted with a delay, producing a recoil force. Since the peak emission occurs around 2 PM local time, the resulting force is oriented near 2 AM, generating an along-track component that causes outward orbital drift (for prograde rotation; retrograde rotation leads to inward drift). (b) Seasonal component: the spin axis lies in the orbital plane. Seasonal heating and cooling of the hemispheres produce a thermal force along the spin axis. Due to thermal inertia, the maximum reradiation occurs after peak insolation (points A and C), namely at B and D, resulting in a net inward orbital drift over one revolution (Bottke et al.,2006 [9]).

This force has a radial outward component and an along-track component, which cause a secular increase in the semi-major axis (orbital expansion) for prograde rotation. Conversely, if the meteoroid rotates in a retrograde sense, the orbit shrinks. If the rotation axis were lying exactly in the orbital plane, the diurnal Yarkovsky effect would be suppressed entirely [9].

The magnitude of the diurnal effect depends on several factors: how close a body is to the Sun, the obliquity of the spin axis, and the body's physical characteristics such as size, shape, thermal properties, and rotation rate. The interplay of these variables implies an optimal size for maximizing the diurnal effect for a given rotation speed and thermal structure. For high-mass objects like planets, the acceleration induced by the Yarkovsky effect is negligible. However, it becomes significant for smaller bodies, ranging from a few centimetres to several kilometers in diameter. For bodies within this size range, the effect is sufficient to modify the orbit, often transporting the object into resonances (such as the 3:1 mean-motion resonance with Jupiter or the ν_6 secular resonance). These resonances deliver the objects into the inner Solar System, effectively modulating the impact risk with Earth. Finally, it is important to note that objects with either zero or infinitely fast rotation rates experience no net diurnal Yarkovsky force, as the temperature distribution remains perfectly symmetric relative to the subsolar point [87] [9].

Description of Seasonal Component

The seasonal component of the Yarkovsky effect arises from the change in solar illumination as the asteroid moves along its orbit, combined with the tilt of its spin axis. As illustrated in Figure 1.2b, unlike the diurnal component, which is maximised when the spin axis is perpendicular to the orbital plane, the seasonal effect is most significant when the spin axis lies in the orbital plane [9].

Consider a meteoroid at position A (bottom of the figure). The Sun shines most intensely on its northern hemisphere. Due to thermal inertia, a heating lag occurs, such that the northern hemisphere reaches its maximum temperature at position B. Similarly, the Sun shines most strongly on the southern hemisphere at C, but this hemisphere becomes hottest at position D. Although the radiation reaction force is symmetrical in Figure 1.2b, the continuous change in the body's velocity vector along the orbit ensures that the net force results in a secular decrease of the semi-major axis. Unlike the diurnal component, which can cause either inward or outward drift depending on the rotation sense, the seasonal component acts as a thermal drag [75] that always causes the orbit to shrink. However, for a body without thermal inertia, the along-track force averages to zero when integrated over one revolution about the Sun [9].

Unlike the diurnal Yarkovsky effect, the seasonal Yarkovsky effect is independent of the sense of rotation of the meteoroid; reversing its spin does not change the effect's sign. Moreover, the relevant timescale for the seasonal effect is the orbital period of the meteoroid rather than the rotational period, which is usually much shorter and is involved in the diurnal effect [9].

1.2.2 The YORP Effect

The emission of thermal radiation affects not only an asteroid's semi-major axis but also its rotational state (period and orientation of the spin axis). This phenomenon is known as the Yarkovsky–O'Keefe–Radzievskii–Paddack (YORP) effect. While the Yarkovsky effect can be modelled using a spherical body, the YORP effect arises specifically from the asymmetrical shape of an asteroid. The YORP effect is a non-gravitational force due to the thermal photon emission from the asteroid surface, and can change the spin of the body if it has the right shape. An asteroid to be spun up must have a certain amount of asymmetry in its shape; figures of revolution, such as the sphere or even the triaxial ellipsoid, will not be affected by the YORP effect [74]. Moreover, the YORP effect is extremely sensitive to surface details, like surface roughness, boulders, and craters. A single large feature can alter YORP by several tens of percent or more [77]. Given that the topographical features of asteroids are known in detail in only a few cases, it is extremely difficult to predict spin-rate evolution in individual cases or in populations of homogeneous bodies [77].
Variations in rotational period due to the YORP effect have already been detected on the asteroids (1862) Apollo, (54509) YORP, and (1620) Geographos [33]. The YORP effect, despite collisional interference, appears to be physically important for the evolution of asteroid rotational properties, at least for objects up to about 40 km in diameter with an average density of $2-3$ g/cm^3. Indeed, the YORP effect could be the driving force behind the large number of slow and fast rotators present among asteroids smaller than 40 km in diameter. It is precisely the rotation periods of these asteroids that cause the significant deviations from the Maxwellian distribution of rotation frequencies predicted by purely collisional theory.

1.2.3 The Poynting-Robertson Effect

The Poynting-Robertson (P-R) effect represents a critical non-gravitational perturbation in the orbital evolution of interplanetary dust particles [73]. This effect tends to cause smaller particles to spiral toward the Sun and, physically, is due to the aberration sunlight undergoes when observed from a body in heliocentric orbit: sunlight arrives slightly from the direction of the particles' motion, slowing its orbital velocity due to momentum transfer from photon to particle that is not counterbalanced by re-emissions. The orbital decay time is directly proportional to the particles' diameter and the square of the orbit's semi-major axis. The secular impact of the P-R effect is the gradual reduction of both the semi-major axis (a) and the eccentricity (e) of the orbit.

For a spherical particle of radius s in a near-circular orbit (i.e, $e \approx 0$) that absorbs all the radiation from the Sun and re-emits this radiation isotropically at the same rate, the time τ_{PR} required to spiral from an initial distance a into the Sun is approximately [92]:

$$\tau_{PR} \approx \frac{4\pi \rho s c^2 a^2}{3L_\odot} \approx 7 \cdot 10^6 \rho\, s\, a^2 \tag{1.4}$$

In Eq. 1.4 ρ is the particle density, and $L_\odot$ is the solar luminosity. In the simplified, more practical version, τ_{PR} is in years, ρ is measured in g/cm^3, s is in cm, and a is in au. This timescale demonstrates that the effect is size-dependent; smaller grains are cleared from the inner solar system significantly faster than larger boulders or asteroids.

The P-R effect acts as an "aspirator" for the zodiacal cloud. Without a continuous replenishment of dust—primarily through cometary activity and collisional grinding in the asteroid belt—the inner solar system would be depleted of circumstellar dust on timescales of 10^4 to 10^6 years. Furthermore, this effect is instrumental in transporting material into mean-motion resonances with planets, leading to the formation of resonant circumsolar rings. Later, we will see the effect this may have on the hypothetical population of Vulcanoids within Mercury's orbit.

1.3 Dynamics and Distribution of Asteroid Populations

The current architecture of the Solar System's minor body populations results from a complex interplay between primordial formation processes and dynamical evolution. These bodies are not isolated groups but are part of a continuous, though structured, distribution that preserves the history of planetary migration and gravitational scattering [60].

The distribution of these populations is primarily governed by gravitational resonances with giant planets and by the non-gravitational effects discussed in the previous sections. Although most asteroids are found in stable reservoirs, they are subject to secular transport mechanisms that can move them into unstable regions, effectively feeding one population from another. Mapping these well-established reservoirs is essential to trace the Solar System's history; however, it also highlights the gaps in our current architecture [80]. Indeed, these same dynamical models [40] [39] predict the existence of primordial stable zones in the extreme inner Solar System, where the elusive Vulcanoid population is theorised to reside.

1.3.1 Kuiper Belt: general characteristics and history

Moving inward from the edge of the Solar System, the first major population of minor bodies is the Kuiper Belt, a vast circumstellar disc of small bodies named in honour of the Dutch astronomer Gerard Kuiper [52]. It extends from the orbit of Neptune at 30 AU, to approximately 55 AU from the Sun. This region, containing ~ 0.01 Earth masses of material [42], is populated by hundreds of thousands of icy bodies, known as Kuiper Belt Objects (KBOs), which are remnants of the Solar System's formation. They are primarily composed of frozen volatiles such as methane, ammonia, and water ice.

KBOs are commonly divided into two dynamical classes, referred to as *cold* and *hot*, although these terms are not related to temperature. Cold KBOs are characterised by nearly circular orbits (i.e., low eccentricities) and low inclinations, meaning that their motion closely follows the ecliptic plane, similarly to the major planets. In contrast, hot KBOs exhibit more eccentric and inclined orbits, resembling in some respects the dynamical behaviour of comets.

This distinction is not merely dynamical but is also reflected in their size distribution. By analysing the absolute magnitude distribution of KBOs through the recalibration of multiple observational surveys, it has been shown that both populations follow a broken power-law, with significantly different slopes for larger bodies. In particular, the hot population appears to share the same size distribution as Jupiter Trojans [42], supporting the predictions of the Nice model and suggesting a common origin linked to planetary migration in the early Solar System. Cold KBOs, however, don't fit this framework. Their size distribution differs, with relatively fewer large objects compared to smaller ones, and appears consistent with formation in situ within a low-density environment. Interestingly, both cold and hot populations show similar behaviour at smaller sizes, diverging only at larger scales, which is difficult to reconcile with a simple formation scenario for the cold population at their present locations.

Beyond the dynamical classification, the architecture of the Kuiper Belt is further defined by mean-motion resonances with Neptune. A significant fraction of the population, known as Resonant KBOs (including the "Plutinos" in the 3:2 resonance), provides a fossil record of Neptune's outward migration [54]. In addition, the abrupt decrease in object density at approximately 50 AU, known as the Kuiper Cliff [84], remains an unresolved mystery that challenges current models of the primordial solar nebula's extent.

These results suggest that the collisional and dynamical evolution of the Kuiper Belt is more complex than previously assumed and cannot be fully explained by standard luminosity function models, raising new questions about planetesimal formation processes in the outer regions of the Solar System.

1.3.2 Main Belt: general characteristics and history

The Main Asteroid Belt is fundamental in reconstructing the origin and the evolution of the Solar System, probably better than the planets themselves. This is because it provides several key constraints that can be used effectively to guide the development, calibration and validation of evolutionary models [60]. These constraints are particularly stringent as the population's distribution and physical properties are extensively documented [60] through ground-based observations, space missions, and meteorite analysis.

As previously mentioned, the Main Asteroid Belt represents the most densely populated region of the Solar System. To date, more than 1.5×10^6 Main-Belt Asteroids (MBAs) have been identified [59]. The largest body in this region is Ceres, which was also the first asteroid to be discovered in 1801 by the Italian astronomer Giuseppe Piazzi [8]. This discovery was followed by that of Pallas in 1802 [26] and Vesta in 1807 [27], which, together with Ceres, are among the largest known asteroids.

For analytical and observational purposes, the Main Belt is commonly subdivided into three regions based on their semi-major axes (a), reflecting differences in orbital dynamics, collisional history, and physical properties. These are the Inner Main Belt Asteroids (IMB), located between $2.00 < a < 2.50$ AU, the Middle Main Belt Asteroids (MMB), with $2.50 < a < 2.82$ AU, and the Outer Main Belt Asteroids (OMB), spanning $2.82 < a < 3.27$ AU [28] [29].

Asteroids move around the Sun in orbits that are perturbed by the presence of the planets, particularly Jupiter, whose powerful gravitational field has prevented the formation of a planet in that region of space, leaving it in a state similar to its primordial condition at the time of the Solar System's formation [19].

Except for Ceres, the sizes of known asteroids in the Main Belt range from a few km to several hundred km. The inner boundary of the belt lies at approximately $2.1 - 2.2$ AU from the Sun, while its outer boundary is at about 3.28 AU. Interior to 2 AU lies the Hungaria asteroid group, whereas the Hilda, a group of about 6000 bodies [86] with similar orbital elements, is located at 3.97 AU. Heliocentric orbital periods range from approximately 2.8 years for the innermost asteroids to about 8 years for the outermost ones [19].

The Main-Belt asteroids and NEAs do not constitute independent populations; rather, they are strongly linked through evolutionary processes and dynamical transport mechanisms, particularly those associated with orbital resonances.

In particular, mean-motion and secular resonances ν_6 with Jupiter and Saturn play a fundamental role in shaping the dynamical structure of the Main Belt. These resonances create regions of orbital instability, known as Kirkwood gaps, which Kirkwood first identified in 1866 [51], where asteroids are progressively removed over time. Objects entering these resonant regions can experience significant increases in orbital eccentricity, eventually being transported onto planet-crossing orbits.

As a result of these mechanisms, the Main Belt serves as the primary source region for NEAs, continuously supplying new objects to the inner Solar System. This dynamical link between the Main Belt and NEAs is supported by both numerical simulations and observational evidence [28].

In addition to gravitational perturbations, non-gravitational effects also play a crucial role in the long-term evolution of asteroid orbits. In particular, thermal forces such as the Yarkovsky effect [88] can produce a gradual drift in the semi-major axis, allowing small bodies to migrate into resonant regions over long timescales. Similarly, the YORP effect [88] can modify asteroids' rotational states, indirectly influencing their dynamical evolution.

These processes are essential for understanding not only the transport of asteroids toward near-Earth space but also the distribution and stability of small bodies in the innermost regions of the Solar System, where extreme thermal and dynamical conditions are expected. Given their fundamental importance, these effects will be discussed in greater detail in Section 1.2.

1.3.3 NEAs: general characteristics and history

Asteroids and comets are classified as Near-Earth Objects (NEOs) if their perihelion [5] is within 1.3 AU of Earth [19]. The terms Near Earth Asteroid (NEA) and Near Earth Comet (NEC) [6] are used more specifically to distinguish between the two types of celestial body. As of 2026, there are approximately 42,000 known NEAs and approximately 100 NECs [48]. Therefore, NEOs are essentially made up of asteroids.

Due to their proximity, NEAs are the Solar System objects that can interact directly with Earth and affect life on our planet, either positively or negatively. On average, a collision with a large asteroid that causes a global catastrophe is estimated to occur once every few million years [64]. However, small NEAs pose a greater immediate threat to Earth because they are more abundant and statistically impact the Earth more frequently than large NEAs, based on the power law distribution of frequency versus size [64] [68].

Since the very beginning of its existence, the Earth has been subjected to several impacts from NEAs. Some theories suggest that in the first billion years of Earth's existence, NEAs and comets delivered ingredients like carbon and water that could have initiated life on Earth, making them important informants about the formation of the Solar System.

Understanding the origin of NEAs, therefore, requires studying the formation and long-term dynamical evolution of the Main Belt, since NEAs are continuously supplied from this region through resonances and other orbital migration processes.

There are different models that aim to explain how the Solar System formed and evolved to what we observe it today. In some models, it is suggested that MBAs formed near where they are currently located [44], while other models, known as Nice model [61] [62] and the Grand Tack model [90] suggest that the asteroids formed in a primordial asteroid belt further away from its current location and were displaced into the current main asteroid region after planetary migration of Jupiter and Saturn.

Anyway, the most accepted models suggest that the NEA population is in a steady state. NEAs have a short dynamical lifetime of only a few million years before they collide with the Sun, a planet, or are ejected from the Solar System [8], but the population is constantly being replenished from asteroids in the Main Belt. MBAs are heated by the Sun and re-radiate the absorbed energy as thermal emission. Because they rotate on their own axis, the afternoon hemisphere generally reaches higher temperatures than the morning hemisphere. As a consequence, the warmer surface emits a greater amount of thermal radiation into space, producing a net recoil force that can cause the asteroid to slowly move either closer to or further from the Sun [19]. This is the so-called Yarkovsky effect [88]. As MBAs move along their semi-major axes, they experience resonant forces with planets like Jupiter and Saturn, which transport them into near-Earth orbits.

[5] The perihelion distance is the distance at which a cosmological body, such as planets or asteroids, is closest to the Sun in its orbit, and it is given by $q = a(1 - e)$, where a is the semi-major axis and e the eccentricity of the orbit.

[6] We refer to those with an orbital period of less than 200 years [19].

Orbital classes of NEAs

The type of orbit that a NEA travels on determines which of these orbital classes it is included in:

- Atira: when their orbit is completely within Earth's orbit. They have an aphelion Q smaller than Earth's perihelion [7]; therefore, $Q < 0.983$ AU. Only 54 of these asteroids are known because they are visible only shortly after sunset or before sunrise.

- Aten: when the orbit is largely internal to that of Earth, with an aphelion greater than Earth's perihelion ($a < 1$ AU; $Q > 0.983$ AU). There are $2,507$ known Aten asteroids. When viewed from the north pole of the ecliptic, these asteroids appear to cross Earth's orbit, which is why they are known as Earth-crossing asteroids. However, due to the inclination of their orbits, it is uncertain whether there is a real intersection in space.

- Apollo: when the orbit is mostly outside Earth's orbit ($a > 1$ AU; $q > 1.017$ AU). Like Atens, Apollos are also Earth-crossing, and there are $16,205$ of them because they are easier to discover because they can be in opposition to the Sun and are therefore observable at night.

- Amor: when the orbit is tangential to the Earth's orbit ($a > 1$ AU; $1.107 < q < 1.3$ AU). There are $12,922$ of these, and they are the easiest to spot as they are generally observable in the middle of the night.

This classification is not permanent because the orbits of NEAs are chaotic, i.e., they are highly sensitive to initial conditions, and the orbital elements [8] that characterise their orbit change as a result of gravitational perturbations exerted by the terrestrial planets, Jupiter and Saturn. These perturbations become more pronounced the closer the asteroid is to a planet. For instance, an asteroid may transition from an Apollo-type orbit to an Amor-type orbit, or vice versa [19].

1.4 Vulcanoid Asteroids

Among the various classes of minor bodies in the Solar System, Vulcanoid asteroids, the core focus of this Master's Thesis, represent a population of particular scientific interest. These objects are a hypothesized population of small, rocky bodies thought to occupy stable orbits interior to that of Mercury, likely dating back to the early stages of planetary formation. A schematic overview of the Vulcanoid Zone relative to other minor body populations in the inner Solar System is illustrated in Figure 1.3.

[7] The aphelion distance is the distance at which the asteroid is furthest from the Sun; it is given by $Q = a\,(1 + e)$, where e is the eccentricity and a the semi-major axis.

[8] There are six elements that characterize the heliocentric orbit of a Solar System body. The semi-major axis (a) and eccentricity (e) describe the geometry of the orbit; the inclination angle (i) and longitude of the ascending node (Ω) indicate the orientation of the orbit's plane relative to the reference plane; and the argument of perihelion (ω) and time (T) at perihelion define the location of the mass in the orbit.

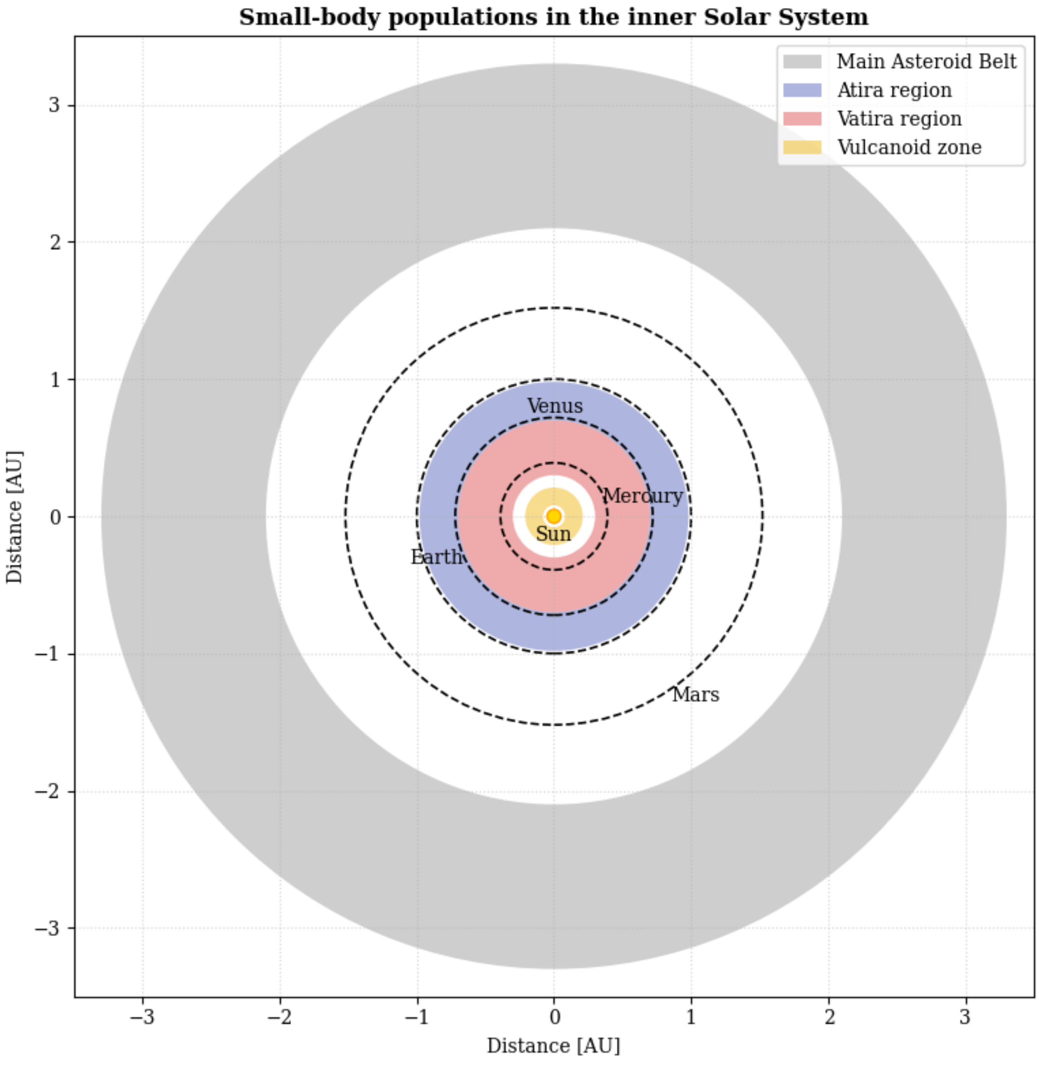

Figure 1.3: Schematic overview of small-body populations in the inner Solar System. The diagram highlights the hypothetical Vulcanoid Zone (yellow) in relation to the Vatira (pink) and Atira (blue) regions, all of which are located interior to the Main Asteroid Belt (grey). The dashed lines represent the orbits of the terrestrial planets.

The so-called Vulcanoid Zone (VZ) is dynamically defined by an outer stability limit of approximately 0.2 AU, beyond which orbital eccentricity is significantly perturbed by gravitational interactions with Mercury and the other terrestrial planets [40]. Small bodies closer to Mercury evolve swiftly into the planet's sphere of influence. Conversely, the inner boundary (at roughly 0.06 AU) is determined by a combination of extreme thermal conditions and non-gravitational transport mechanisms [89], most notably Poynting-Robertson drag and the Yarkovsky effect, which lead to the gradual depletion of smaller debris. The efficiency of P-R mechanism is highly dependent on the particle size, as expressed by the linear dependence on s in Eq. 1.4. As shown in Figure 1.4, for an object located the outer edge of the Vulcanoid Zone ($a = 0.2$ AU) with a typical chondritic density of 3.5 g/cm^3, the decay timescale τ_{PR} varies by several orders of magnitude in response to the object's diameter. The plot reveals a critical threshold: bodies with a diameter $D < 100$ m exhibit a decay time shorter than the age of the Solar System. Consequently, any primordial population of Vulcanoids currently occupying the VZ must consist of kilometer-scale objects, as smaller fragments would have been systematically swept into the Sun unless recently replenished by collisional events.

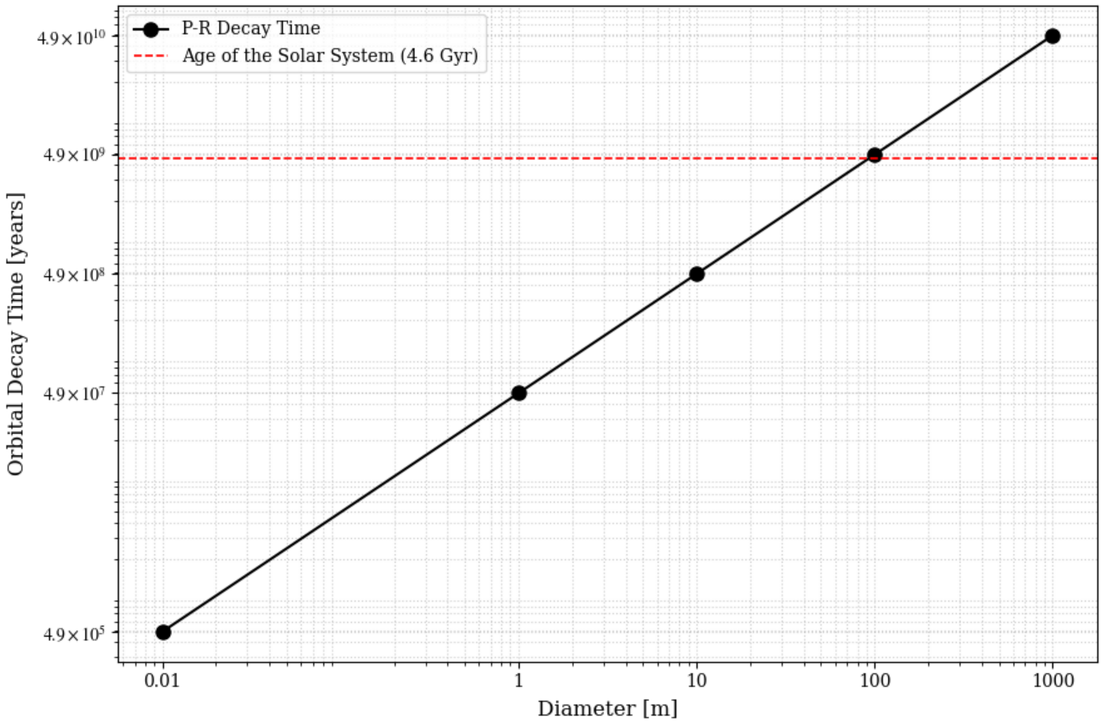

Figure 1.4: Orbital decay time τ_{PR} due to the Poynting-Robertson effect as a function of object's diameter, calculated according to Eq. 1.4. The simulation assumes an initial circular orbit at 0.2 AU and a bulk density of 3.5 g/cm^3. The horizontal dashed line marks the age of the Solar System ($\sim 4.6 \times 10^9$ yr). The linear slope of the curve reflects the direct proportionality between the decay time and the radius of the body. Objects below the ~ 100 m threshold are expected to be removed within the Solar System's lifetime, while kilometer-sized objects remain unaffected by P-R drag.

Despite their theoretical significance, Vulcanoids remain elusive. Their study is characterised by significant observational challenges due to their proximity to the Sun and a complex dynamical evolution driven by intense solar radiation. Nevertheless, detecting these intra-Mercurial objects would offer insights into the primordial environment and thermal history of the inner Solar System.

1.5 Original Contributions of the Thesis

This work aims to provide a comprehensive *state of the art* review of this intra-Mercurial objects research, synthesising past theoretical foundations, current observational constraints, and future perspectives for their discovery during future Total Solar Eclipses (TSEs). Within this framework, the original contributions of this Master's Thesis are:

- Produced a comprehensive review of current constraints on Vulcanoid detection;
- Evaluation of the feasibility of observing Vulcanoids during TSEs;
- Developed a Signal-to-Noise Ratio (SNR) model specific to this challenging observational environment;
- Performed a climatological analysis for the upcoming TSEs of August 12, 2026, and August 2, 2027;
- Design of an observing strategy, including optical systems and acquisition techniques.

To this end, the thesis is structured as follows: Chapter 2 explores the historical context of intra-Mercurial bodies, tracing the evolution of the field from Le Verrier's early perturbation studies to the hypothesis of the planet Vulcan. Chapter 3 examines the dynamical environment of the Vulcanoid stability region, discussing why these objects could remain trapped in such close proximity to the Sun for ages of the order of 4.5 Gyr. In Chapter 4, the main observational challenges associated with the detection of Vulcanoids are presented, including a detailed Signal-to-Noise analysis relevant for observations during solar eclipses. Building on this investigation, Chapter 5 introduces the preliminary observational campaign planned for the Total Solar Eclipse (TSE) of August 12, 2026, in Spain. This event will serve as a crucial dry run to validate the experimental setup, evaluate atmospheric extinction, and test the logistical framework for the upcoming TSE of August 2, 2027, in North Africa. Consequently, Chapter 6 presents the definitive observational mission campaign detailing the optimised optical systems, detectors, and acquisition strategies proposed for the main search. Finally, Chapter 7 summarises the findings and discusses the implications of a potential discovery, or the continued absence, of Vulcanoids for our understanding of the early Solar System's formation.

Chapter 2

History of Intra-Mercurial Bodies' Origin

There are eight known planets in the Solar System, from Mercury to the distant Neptune. Beyond this lies the Kuiper Belt, a reservoir of icy minor bodies surrounding the Solar System. Until 1992, the Kuiper Belt had only been hypothesised, but that year, with the discovery of 1992 QB1 (now known as 15760 Albion), the first evidence of its existence was obtained. What do we have at the inner edge of the Solar System? The planet Mercury, the first protagonist of this historical investigation. It is a celestial body that moves in an elliptical orbit around the Sun with a semi-major axis of 0.39 AU (1 AU = 150 million km), an eccentricity of 0.20, and a sidereal orbital period of 87.97 days. With a diameter of 4,880 km, it is the smallest planet in the Solar System; it has no atmosphere, and its heavily cratered surface is very similar to that of the Moon. As a planet, Mercury is visible to the naked eye; in fact, it was already known to the ancient Greeks, who identified it with Hermes, the messenger of the gods, due to its rapid movement across the sky. The difficulty in observing Mercury with the naked eye is that it never moves very far from the Sun, so it can only be seen shortly after sunset or just before sunrise, when the sky is still clear. Given its highly elliptical orbit, its maximum elongation from the Sun can vary from 18° to 28°: under ideal conditions, it can be observed about 2 hours after sunset.

Just as the discovery of the Kuiper Belt expanded our knowledge of boundaries of the Solar System, the intra-Mercurial region could help us to define its innermost limits. Historically, this investigation was ignited by a detected discrepancy in Mercury's perihelion precession, an orbital anomaly that suggested the presence of unseen mass within the depths of the inner solar environment.

2.1 Le Verrier and Mercury's orbit

The second protagonist is the French astronomer and mathematician Urbain Jean Joseph Le Verrier (1811-1877), famous for the "desktop" discovery of the planet Neptune, which occurred at the Berlin Observatory on September 23, 1846, based on the analysis of gravitational perturbations in the orbit of Uranus. After the discovery of the eighth planet of the Solar System, Le Verrier devoted himself to the study of Mercury's orbit. Le Verrier knew that studying Mercury's orbit was a crucial test for the theory of gravity. Newton's equations would have to be shown to be valid even in those parts of the Solar System where gravity is strongest. The Parisian astronomer then collected all available data on the small planet, covering 400 positions measured with the Paris Observatory's meridian circle and 12 transits of Mercury observed between 1697 and 1832. In 1859, Le Verrier published the results of his research. According to Le Verrier's calculations, the precession of Mercury's perihelion, taking into account the gravitational perturbations exerted by the other planets, which accounted for approximately 527 arcsec/century out of the total deduced advancement of 565 arcsec/century [5], could not be completely explained by Newtonian gravitation; an anomalous excess of approximately 38 arcsec/century (reckoned to be 43 arcsec/century in the modern era) remained.

Perihelion, the point of closest approach to the Sun in a planet's orbit, occurs slightly earlier each year than the previous year, and this is true for all planets and is well predicted by Newtonian mechanics. The precession arises because a perfectly closed elliptical orbit is an ideal two-body solution of Newtonian mechanics. But in the real system, there are many other bodies, primarily the gas giants Jupiter and Saturn, which perturb Mercury's orbit away from a perfect Keplerian ellipse. The result is that the entire orbit rotates slightly on itself as the planet revolves around the Sun, and the perihelion advances each year slightly. All planets therefore have their own degree of precession, but Mercury's was excessive, beyond what could be attributed solely to the other planets.

2.2 The Hypothetical Planet Vulcan

To explain this excess, Le Verrier suggested, among other possible explanations, including a potential underestimation of Venus's mass [63], that the cause of Mercury's anomalous precession of the perihelion was due to gravitational perturbations exerted by another planet (or a series of smaller bodies) in an orbit internal to Mercury's. The successful discovery of Neptune led astronomers to place some confidence in this possible explanation, and the hypothetical planet was named Vulcan by the French physicist Jacques Babinet [1] [4].

The hypothetical planet would have had a mass of order 1/17 th that of Mercury, corresponding to a diameter of 1900 km [5]. Located at an assumed distance of 0.14 astronomical units (AU) from the Sun [5] it would never have risen more than 10 degrees above the horizon, blending in with the last light of sunset or the first light of dawn. On the other hand, being closer to the Sun, it would have reflected more light and therefore shone much brighter than Mercury. One wondered, therefore, how it had managed to escape detection until now. As difficult a planet as it was to see, with all the observations accumulated over the centuries of sunspots, eclipses, and transits of Mercury and Venus, it was hard to imagine anyone had even accidentally spotted it.

On December 22, 1859, just three months after Le Verrier's presentation to the Academy of Sciences, Edmond Modeste Lescarbault, a French physician and amateur astronomer, wrote a letter to Le Verrier in which he told him that the intra-Mercurial planet really existed; he had seen it during a transit the previous March. It was March 26, around four in the afternoon, when Lescarbault saw a small, round spot

[1] Although Mercury is the first planet in the Solar System according to the Titius-Bode law [7] [6] [65], modifications proposed by Jenkins [49] would allow the existence of an additional planet between Mercury and the Sun.

in the upper part of the solar disc, about a quarter the size of Mercury, and, more importantly, moving. It was not a sunspot since sunspots move slowly, rotating with the Sun, whereas the motion of that round spot was much faster. On January 2, 1860, Le Verrier reported the story to the Academy of Sciences in Paris, and the planet was given the name Vulcan, the god of fire, as proposed by Babinet. However, not all were convinced. Emmanuel Liais, observing from Rio de Janeiro with a telescope twice as powerful, reported no such transit at the time claimed by Lescarbault and publicly disputed the observation [4] [34]. Using data provided by Lescarbault, Le Verrier placed Vulcan at 0.147 astronomical units from the Sun. It would therefore have orbited in just 19 days and 17 hours, with an orbit inclined 12° to the plane of the ecliptic. Under these assumptions, the planet would have moved away from the Sun by a maximum of 8°. By its nature, Vulcan must have been dimmer than Mercury: only in this way could the fact that no one had ever seen it before be explained. The planet would have been expected to transit the Sun between two and four times a year, in the first weeks of spring and autumn. However, Vulcan was not visible during the total solar eclipse of the summer of 1860, observed from Spain, which was followed by Iberian astronomers. No evidence of Vulcan was found, and scepticism grew.

Numerous amateur astronomers reported unexplained transits, including F.A.R. Russell in London on January 29, 1860, and American observer Richard Covington around the same time. In 1862, amateur astronomer Mr Lummis in Manchester claimed another transit, supported by his colleague. Based on these reports, French astronomers Benjamin Valz and Rodolphe Radau calculated Vulcan's orbital period: 17 days and 13 hours, and 19 days and 22 hours, respectively [34]. Another report came from Aristide Coumbary in Istanbul on May 8, 1865. Despite these claims, no reliable observations were made from 1866 to 1878.

During the total solar eclipse of July 29, 1878, two seasoned astronomers (James Craig Watson, observing from Separation Point, Wyoming, and Lewis Swift, stationed near Denver, Colorado) independently claimed to have sighted a planetary body in close proximity to the Sun. Watson reported seeing two "strange reddish stars" [4] [76] approximately 2.5° southwest of the solar disc, which he identifies as intra-Mercurial bodies with an estimated magnitude of 4.5.

Swift, for his part, attributed his discovery to a fortunate technical mishap: he had in fact forgotten to untie a rope securing a long pole to his telescope, a trick used to prevent wind vibrations. This limitation forced Swift to sweep the sky toward the west, unexpectedly leading to his discovery [81]. During the total phase, he spotted two large, round, red stars of equal brightness (estimated at magnitude 5) situated about 3 degrees southwest of the Sun. He observed these objects three times before a passing cloud obscured his final view. The two bodies were separated by about 7 or 8 arcminutes, forming a line pointing directly toward the centre of the Sun. At the time, Swift was unable to distinguish which of the two was the reference star (θ Cancri) and which was the planet Vulcan. It was only after consulting with Watson that the enigma was clarified, with Watson specifying that "the planet was the one nearest the Sun". Using the coordinates for θ Cancri provided by the Astronomer Royal, Swift calculated the planet's position at RA 8h 26m 40s and Dec +18° 30' 25", a result remarkably close to Watson's data [81]. However, they disagreed on the orbital mechanics: while Watson believed the planet was approaching its superior conjunction, Swift concluded it had likely just passed its inferior conjunction.

However, no other observers confirmed these findings; in fact, the observations were criticised by several astronomers, among them C. H. F. Peters of Clinton College [76], who questioned their reliability.

Despite this professional scepticism and the fact that the objects were never recovered in subsequent searches, Watson remained absolutely convinced of his discovery. This conviction turned into a lifelong obsession: in 1879, he moved from Ann Arbor to Madison, partly motivated by the prospect of using superior instruments to continue his search. At the time of his unexpected death in 1880, Watson was even in the process of constructing an underground solar observatory, a specialised structure through which he hoped to observe Vulcan in broad daylight [76]. Although it is now established that Vulcan does not exist, Watson's observations at the July 1878 eclipse remain a subject of historical interest; it is probable that he observed at least one, and possibly two, pygmy comets in the vicinity of the Sun [76].

While astronomers like Watson and Swift were searching for intra-Mercurial objects, others were focused on capturing the first photographic records of the event. In Denver, Colorado, Gustav A. Goehner, a German immigrant who took advantage of the high altitude and cloudless skies, documented the eclipse's progression with remarkable precision, eventually producing a miniature souvenir book of his observations (Figure 2.1a). Each image, measuring approximately 6.5 × 6.5 cm, includes a timestamped caption, allowing the viewer to experience the moon's passage minute by minute. His work, which culminates with the capture of the glowing solar corona during totality at 3:29 p.m. (Figure 2.1b), remains a significant historical and artistic artefact of the 1878 eclipse [43].

Following the controversial 1878 observations, the search continued through subsequent solar eclipses in 1882, 1901, and 1905, yet each expedition failed to provide conclusive evidence of Vulcan's existence [70] [71]. The definitive turning point came in 1909; following the results of the Crocker Expeditions (which included the 1908 solar eclipse), William Wallace Campbell and Charles Dillon Perrine stated [17]:

> *"In our opinion, the work of the three Crocker Expeditions, to observe the eclipses of 1901, 1905, and 1908, brings the observational side of the intramercurial planet problem, famous for half a century, definitely to a close."*

This declaration officially marked the end of the Vulcan era as a major planetary body. By employing long-exposure photography, a method far more reliable and objective than the visual observations of the previous century, Campbell and Perrine [71] demonstrated that no object brighter than magnitude 8.0 or 9.0 existed in the Sun's vicinity. With the observational search for a large planet exhausted, the theoretical mystery was finally resolved in 1915. Albert Einstein's General Theory of Relativity explained Mercury's anomalous precession as a relativistic effect of spacetime curvature near the Sun [35] [4], rendering the existence of a perturbing planet unnecessary.

Although the hypothetical planet Vulcan does not exist, the search for a ring of small bodies between the orbits of Mercury and the Sun has not been abandoned and continues: these are the Vulcanoid asteroids, named after the planet theorised by Le Verrier.

(a) The complete miniature souvenir book showing the accordion foldout of the photographic prints.

(b) Detail of the telescopic view at 3:29 p.m., documenting the moment of totality.

Figure 2.1: Photographic documentation of the total solar eclipse of July 29, 1878, by Gustav Adolph Goehner.

Chapter 3

The Vulcanoid Stability Region

Our understanding of the architecture of the Solar System has grown significantly in recent decades, including the discovery and characterisation of the various asteroid populations discussed in Section 1.3. The study of these populations has provided fundamental insights into the nature and origins of minor bodies throughout the Solar System. Among the few stable dynamical niches that remain largely unexplored today is the region interior to Mercury's orbit, where the Vulcanoids are hypothesised to reside.

This chapter analyses the dynamical and thermal environment of the Vulcanoid region. It discusses the orbital boundaries of this stability zone, the non-gravitational perturbative effects, and the hypotheses about the collisional evolution of a potential primordial population.

3.1 Orbital Definition and Boundaries

For over a century, astronomers have hypothesised the presence of asteroids residing in the dynamically stable region interior to Mercury's orbit. This region, known as the Vulcanoid Zone (VZ), is dynamically defined as the circumsolar space bounded by the silicate sublimation limit and the orbit of Mercury.

However, the exact boundaries of the VZ are not uniquely defined in the literature but rather complex thresholds determined by the balance between gravitational stability and destructive thermal and radiative forces. Over the years, these boundaries have been refined by theoretical advances and by the photometric limits of observations.

3.1.1 Physical and Dynamical Limits

The theoretical extent of the VZ is constrained by two primary boundary mechanisms: thermal evaporation and dynamical instability.

- **The Inner Boundary ($\sim 0.06 - 0.09$ AU):** This limit is strictly defined by a combination of extreme solar heat and radiative transport forces. At a heliocentric distance of 0.06 AU, solar insolation is so intense that even a hypothetical iron body 100 km in diameter would entirely evaporate within the lifetime of the Solar System [78] [18]. Slightly further out, at $0.07 - 0.08$ AU, non-gravitational forces such as Poynting-Robertson drag, and the Yarkovsky effect rapidly force smaller collisional fragments to spiral inward toward the Sun, leading to their vaporization [78] [80] [89].

- **The Outer Boundary ($\sim 0.18 - 0.21$ AU):** This boundary is established by gravitational instability [78]. Beyond 0.21 AU, the combined gravitational perturbations from Venus and the highly eccentric orbit of Mercury rapidly destabilise and eject any asteroid from the zone [57] [80].

Because of these combined effects, the actual "safe range" for Vulcanoids is narrower than the extreme physical limits. In 1999, in an article published in *Nature* by Evans and Tabachnik [40], it was demonstrated through numerical simulation that the region in which planetesimals with a radius greater than 0.1 km can survive for a time comparable to the age of the Solar System lies between 0.09 and 0.21 AU from the Sun. Long-term stable orbits are found only within this range of heliocentric distances.

The heliocentric range $0.09 - 0.21$ AU corresponds to maximum solar elongations between 5.1° and 12°. Considering that it is already difficult to observe Mercury at sunset or just before sunrise because of the bright sky, it is easy to understand how challenging it is to search for Vulcanoid asteroids with a telescope.

3.1.2 Observational and Photometric Constraints

Because of the extreme proximity to the Sun, observational searches must be conducted through the bright twilight glare, during rare Total Solar Eclipses (TSEs), or from space. As a result, the assumed boundaries and the maximum size of a potential Vulcanoid population have been progressively constrained by the photometric limits of the instruments used to probe the region.

Converting an instrumental limiting magnitude into a physical diameter for a Vulcanoid is not a simple conversion; it depends on the assumptions regarding the object's heliocentric distance, its surface albedo, and its phase function [80]. As demonstrated by Durda et al. [32], a constant limiting magnitude of $V = 8.0$ can be used to rule out objects larger than 20 km in diameter at the inner edge of the Vulcanoid Zone. However, at the outer edge, the same photometric limit can only rule out objects larger than 60 km [32] [78].

Consequently, the theoretical upper limits on the Vulcanoid population's size distribution and total mass have been progressively lowered over the decades as detector sensitivity has improved. The specific observational campaigns that established these limits, evolving from early ground-based eclipse photography to modern space-based coronagraphs and planetary probes, along with the intrinsic signal-to-noise challenges of detecting these faint bodies, are detailed in Chapter 4.

3.1.3 Dynamical Stability

The theoretical boundaries of the Vulcanoid Zone (VZ), in its maximum extent as derived from the literature, are defined by a combination of dynamical and thermodynamic constraints. The maximum VZ stability region extends from a sublimation-driven inner limit of 0.06 AU [80] to an outer limit of 0.25 AU set by planetary perturbations [18], with orbital inclinations up to 15° [78] [32] [67]. However, the stability within this belt is not continuous. As illustrated in Figure 3.1 that I adapted from

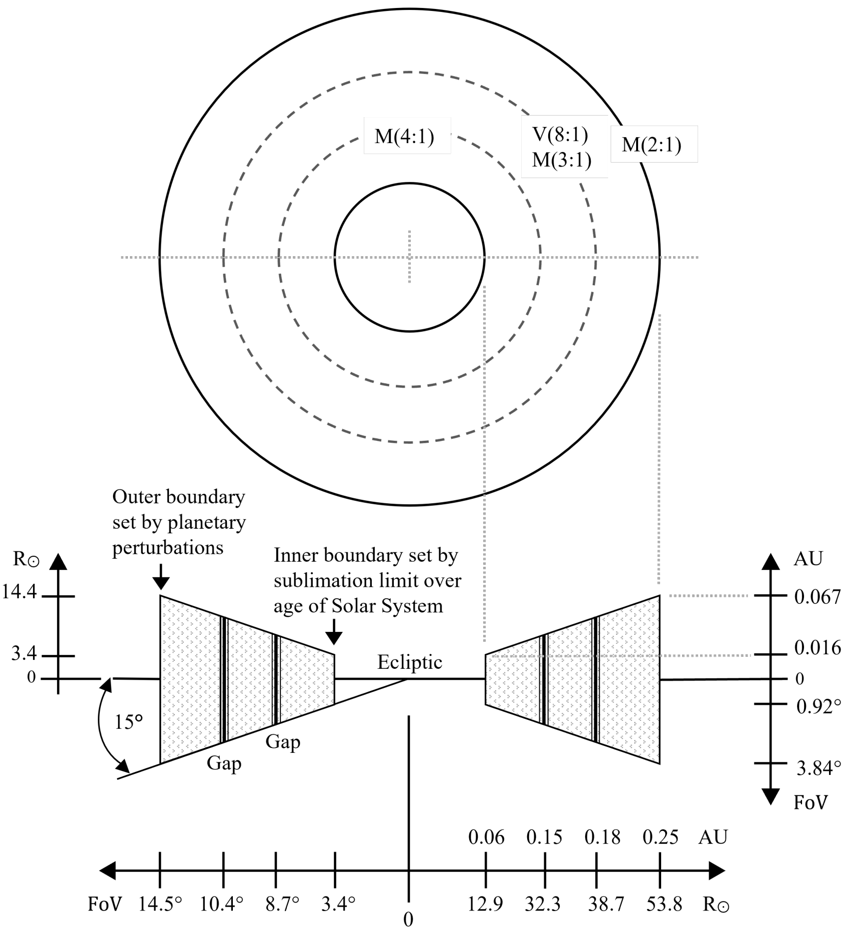

Figure 3.1: Schematic of the maximum Vulcanoid Zone stability regions. Top: polar view showing the locations of the main mean-motion resonances with Mercury (M) and Venus (V), indicated by dashed lines. Bottom: cross-section relative to the ecliptic plane, highlighting the inner boundary (set by the sublimation limit) and outer boundary (planetary perturbations), the estimated maximum inclination of 15°, and the gaps corresponding to forbidden orbits. The axes display the distances in Astronomical Unit (AU), solar radii ($R_\odot = 6.957 \times 10^8$ m [55]), and the corresponding angular elongation in degrees as seen from Earth, calculated from the heliocentric distance.

Peltier (2019) [67], "even within this region, there are 'forbidden orbits', for example at 0.15 and 0.18 AU, corresponding to mean-motion resonances with Mercury and Venus" [40] [39]. These gravitational interactions create actual gaps (similar to the Kirkwood gaps in the Main Asteroid Belt), fragmenting the stability zone and defining the complex dynamical architecture in which any potential Vulcanoid bodies might reside.

Beyond planetary gravity, non-gravitational forces strongly affect the lifetimes of hypothetical Vulcanoids; sublimation, surface fracturing, the Poynting-Robertson effect, and the diurnal and seasonal Yarkovsky effects must also be considered.

The Poynting-Robertson effect causes smaller asteroids to spiral toward the Sun and arises from the aberration of sunlight as seen in the asteroid's rest frame: radiation appears to come slightly from the direction of motion, reducing the orbital velocity. The orbital decay time is directly proportional to the asteroid's diameter and to the square of the semi-major axis. For asteroids with a diameter of 50 m at 0.15 AU, the decay time is comparable to the current age of the Solar System. In contrast, for bodies of 1 km it reaches $\sim$32 Gyr, rendering their orbits effectively stable.

The Yarkovsky effect arises from the recoil force due to anisotropic thermal emission from a rotating body. It consists of two components: diurnal and seasonal. The diurnal component is associated with the asteroid's rotation and, depending on the spin direction, can either increase or decrease the semi-major axis. The seasonal component, instead, is due to the revolution around the Sun and always decreases the orbital radius. For small, rapidly rotating asteroids, the seasonal effect dominates, since the surface does not have time to cool during the night. In this regime, the Yarkovsky effect can either counteract or enhance the Poynting-Robertson drag. For a 1 km asteroid with a rotation period of 5 h at 0.15 AU and an obliquity of 45°, the decay timescale associated with the seasonal Yarkovsky effect is of the order of 2 Gyr.

3.2 Thermal Environment and Surface Temperatures

In addition to dynamical perturbations, the extreme radiation environment imposes stringent physical constraints on the existence of Vulcanoids. Sublimation and surface fracturing are caused by the high temperatures and thermal cycling experienced by these bodies [5].

Assuming a Bond albedo of 0.2 (i.e., only 20% of solar radiation is reflected back into space, while the rest is absorbed, increasing the body's temperature), an emissivity of 0.9, and an orbital radius of 0.15 AU [5], the equilibrium temperature is about 700 K, which can lead to surface sublimation. Although modest on short timescales, this mass loss becomes critical over the $\sim$4.56 Gyr lifetime of the Solar System. Furthermore, stellar models reveal that the Sun's luminosity has increased by 25% to 30% over its Main Sequence (MS) lifetime [1] [5]. Taking into account this lower luminosity in the past, sublimation models imply that a stony (fayalite) Vulcanoid, located near the inner edge of the stability zone, must have had an initial diameter of at least 15 km to survive to the present day against evaporation [5]. This extreme thermal environment not only threatens their survival but also dictates how we must search for them. As illustrated in Figure 3.2, assuming a theoretical baseline Bond albedo of 0.2, the thermal emission of such a heated body peaks in the mid-infrared. This provides a unique spectral signature that can be exploited to mitigate the overwhelming glare of the scattered solar spectrum and the coronal background.

These thermal properties have guided various search strategies: Zhao et al. [95] used an RG10 filter in the visible/near-infrared to minimise blue sky light and the green wavelength of the solar corona, taking advantage of the fact that a potential Vulcanoid would be hotter than Mercury. Previously, Leake et al. [53] historically attempted the search using the L-band at 3.5 μm, optimised to exploit the high thermal emission peak (up to 850 K for objects closer than 0.1 AU) in broad daylight to overcome the daytime sky brightness, while, more recently, the WB-57 airborne mission by Caspi et al. [21] has opened up incredible future scenarios, having successfully tested scientific cameras with actively cooled InSb sensors sensitive specifically

[1] The MS phase is characterised by hydrogen fusion in the stellar core; as hydrogen is depleted, the core becomes denser, slowly contracting and heating up to maintain hydrostatic equilibrium. This accelerates nuclear reactions, steadily increasing the star's luminosity.

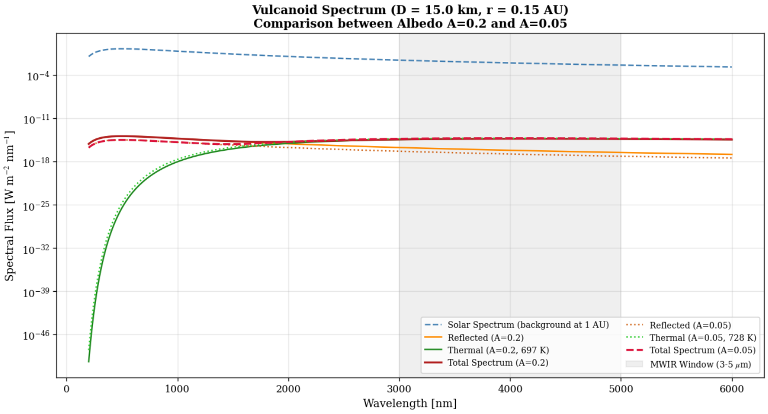

Figure 3.2: Spectral flux distribution for a hypothetical Vulcanoid with a diameter of $D = 15.0\,\text{km}$, located at a heliocentric distance of $r = 0.15\,\text{AU}$, and observed at a standard distance of $\Delta = 1\,\text{AU}$. The model compares two scenarios: a theoretical baseline geometric albedo of $A = 0.20$ resulting in a radiative equilibrium temperature of 697 K and a darker body with $A = 0.05$ (resulting in 728 K. The dashed blue curve represents the reference solar spectrum at 1 AU. At visible and short near-infrared wavelengths ($\lambda < 1.5\,\mu$m), the object's signal is entirely dominated by reflected solar light (solid orange curve for $A = 0.2$ and dotted orange curve for $A = 0.05$). However, in the mid-infrared region (grey shaded band), the object's intrinsic thermal emission (green curves) completely overtakes the reflected component. Consequently, the wavelength region $3 - 5\,\mu$m represents an ideal observational window from the ground for thermal observations, since the total flux of the object (red curves) is entirely dominated by its intrinsic thermal contribution in both scenarios, effectively minimising the background noise associated with solar reflection.

to the $3 - 5\,\mu$m (MWIR) range, the exact interval where the 700 K emission peak resides. While ground-based infrared observations are heavily limited by atmospheric water vapour absorption, stratospheric or space-based platforms can fully exploit this window to isolate the Vulcanoid's emission against the solar corona.

3.3 Primordial Population Hypotheses

The current Vulcanoid population, if it exists, is probably a small remnant of a hypothetical primordial Vulcanoid population, due to the combined effects of collisional evolution and subsequent radiative transport of collisional fragments.

Cosmogonical models suggest that this primordial population could have originated as a natural product of terrestrial planet formation. For instance, the aerodynamic drag inn the solar nebula could have caused a density-dependent fractionation of planetesimals, leaving an iron-rich residue in Mercury's zone and at smaller heliocentric distances. Alternatively, as hypothesised by Wetherill [91] and Cameron [15] in 1986, if Mercury's high iron-to-silicate ratio is the result of a catastrophic impact that stripped away its primordial silicate mantle, Vulcanoids could be the fragments of proto-Mercury's mantle or debris from other collisions in that region.

The existence of a primordial Vulcanoid population was also proposed as an alternative solution to the paradox of Mercury's cratering chronology [53]. Traditionally, the chronology of Mercury's craters was assumed to date back to the Late Heavy Bombardment (LHB), a period of intense asteroid impacts that occurred during a narrow interval between 3.92 and 3.85 billion years ago [82]. However, this assumption conflicts with the planet's thermal and geophysical models. Mercury has an active global magnetic field, implying that its core is still partially molten [2]. Furthermore, if core formation had occurred late in the planet's history, the associated heating and expansion would have erased all previously formed craters.

To reconcile these geophysical constraints, Leake et al. [53] suggest that Mercury's craters might not have been caused by the same impactor populations that bombarded the Moon, instead they could be the results of a prolonged bombardment by Vulcanoids. Because their orbits would only occasionally cross that of Mercury, Vulcanoids would have a longer dynamical lifetime, potentially extending the cratering epoch well beyond the lunar LHB. This would imply that Mercury's surface is younger than the Moon's, providing the time needed for early core formation without subsequent obliteration of the cratering record. In addition, Vulcanoids would impact at relatively low velocity (around 20 km/s) and would not be scattered outward to leave traces on the Moon or other terrestrial planets.

Finally, while the Vulcanoid hypothesis offers a mechanism to modestly extend Mercury's cratering chronology, dynamical models show it is insufficient to completely resolve the thermal paradox on its own [53]. Consequently, it is now believed that Mercury's core must contain a significant fraction of light elements, such as sulfur, which lowers the melting point of the iron core and prevents its total solidification.

3.4 Collisional Evolution and Population Depletion Models

As previously mentioned, the collisional evolution in the Vulcanoid Zone has important implications for present-day population constraints. Although the orbital dynamics of this region allow for the existence of small rocky bodies between 0.06 and 0.21 AU from the Sun [40], this environment is characterised by extremely energetic collisions that tend to shatter objects rather than favour their accretion [80]. Due to the high Keplerian orbital velocities close to the Sun, collisions in the VZ are highly erosive. Assuming a swarm of objects in approximate statistical equilibrium, where the mean random inclination is $\langle i \rangle = \frac{1}{2} \langle e \rangle$, the mean encounter speed at infinity (V_{enc}) as a function of the heliocentric semi-major axis a is given by [80]:

$$V_{enc} = 180 \langle e \rangle \sqrt{\frac{0.1 \text{ AU}}{a}} \text{ km s}^{-1} \tag{3.1}$$

Even for a relatively low mean orbital eccentricity $\langle e \rangle = 0.01$, the encounter speed is approximately 2 km s^{-1}. This value is over an order of magnitude higher than the escape velocity (0.1 km s^{-1}) of a 50-km-radius body with a density equal to the Earth's iron core [80]. Consequently, impacts inevitably lead to a net loss of mass. This transition between accretion and erosion is defined by a critical eccentricity (e^*) [79]. For the VZ, e^* is extremely low: objects with radii of a few kilometers or less will suffer

[2] If the core had completely solidified over this time, it would have caused a global radial contraction of approximately 17 km. However, the observed lobate scarps on the surface suggest a global contraction of only $1 - 2$ km.

erosion if the orbital eccentricities are as low as 5×10^{-5} to 10^{-3}, depending on their mechanical properties and heliocentric distance [80].

This highly erosive environment has direct consequences for the theoretical cratering rate on Mercury. As demonstrated by early collisional models [53], populations of bodies near Mercury's orbit undergo rapid collisional exhaustion on timescales of 0.5 to 1.0 Gyr. This progressive destruction significantly limits the role of Vulcanoids in forming the craters visible on Mercury's surface. Because the population depletes so rapidly, Vulcanoids impacts could not have provided a continuous source of cratering over the Solar System's history; instead, they contributed only to slightly prolonging the initial period of heavy bombardment [53].

To quantify the depletion of this theoretical population, Stern and Durda [80] employed a static, multi-zone collision rate model (CRM) based on a particle-in-a-box (PIB) statistical formalism. The mean collision time t_{coll} on a target of cross-section σ is calculated as:

$$t_{coll} = (n\sigma v)^{-1} \tag{3.2}$$

where n is the projectile number density and v is the mean random speed of the projectiles. Assuming a VZ populated by 10^4 projectiles with a radius > 0.1 km and an eccentricity of 10%, the mean time between collisions for a 3-km target is approximately 350 Myr, dropping to just 3.5 Myr for a 30-km target. This static model demonstrated that virtually no primordial objects in the 1 to 25 km radius range could survive for 4.5 Gyr [80].

To observe the progressive destruction of these bodies, they also ran time-dependent collisional evolution simulations using a Lagrangian "moving bin" approach. The specific impact energy Q^* for a collision pair is computed as:

$$Q^* = \frac{1}{2}\frac{m_k v_{kl}^2}{m_l} \tag{3.3}$$

where m_k and m_l are the masses of the colliding bodies ($m_k < m_l$) and v_{kl} is their relative speed. When Q^* exceeds the catastrophic disruption threshold Q^*_D, the target is shattered. The median fragment speed v_{med} is strictly dependent on the kinetic energy fraction (f_{KE}), assumed to be 10% ($f_{KE} = 0.10$), according to the relation $v_{med} = \sqrt{2 f_{KE} Q^*}$ [80].

The numerical simulations yielded drastic results: even assuming an initial, massive primordial population similar to the present-day Asteroid Belt (with a total mass of $9\times10^{-4} M_\oplus$ [3] and objects up to 330 km in radius), such an ensemble would be pulverised in just 18 to 45 million years (approximately 1% of the age of the Solar System) if the mean random eccentricity exceeded $\sim 3 \times 10^{-3}$ [80].

These numerical simulations show that the primordial population has been drastically reduced over time due to continuous collisional grinding. The survival of debris is further prevented by rapid dynamical transport mechanisms that drag the dust into the Sun, effectively cleaning the region [80]. Consequently, despite the potential dynamical stability of the region [40], current models suggest the Vulcanoid Zone is plausibly almost entirely devoid of kilometer-scale or larger objects.

[3] $M_\oplus \approx 5.9722\times10^{24}$ kg [72] is the Earth mass; its first accurate estimation was historically achieved by Cavendish [22] in 1798.

However, the efficiency of these long-term orbital mechanisms, specifically thermal forces such as the Yarkovsky effect [87] and the Poynting-Robertson drag, also depends on changes in spin-axis orientation and surface properties, making it difficult to derive general conclusions. Therefore, the existence of Vulcanoids cannot be ruled out on purely theoretical grounds and must be investigated observationally.

Chapter 4

Observational Constraints and Detection Challenges

Despite the severe observational limitations and the hostile environment near the Sun, the search for Vulcanoids has motivated observational campaigns for more than a century. Observational strategies have progressively evolved with technological advances, transitioning from early ground-based observations by astronomers such as Perrine and Campbell to modern space-based expeditions. In this context, researchers including Durda, Stern, and Steffl established the most rigorous constraints to date on the Vulcanoid population by bypassing Earth's atmosphere using space-borne instruments such as the SOHO and STEREO space telescopes, representing a significant improvement in observational sensitivity.

Alongside these space missions, total solar eclipses remain a highly effective and accessible alternative for ground-based searches. Among modern eclipse campaigns, the work of Zhao et al. during the 2008 solar eclipse provided stringent observational limits achieved during totality.

This chapter reviews the history and technological evolution of these observational campaigns. By detailing the methods, the instruments, and the major limits obtained so far, this section outlines the current constraints on the Vulcanoid population and the state of the art in this research field.

4.1 Early Ground-based Searches

As far as we know, Perrine's 1902 work [70] represented one of the first attempts to identify intra-Mercurial objects using cameras of notable focal length through terrestrial observations, motivated by the effort to explain the anomaly in the motion of Mercury's line of apsides discovered by Le Verrier [70]. To overcome the limitations of previous searches, which relied on a purely visual approach highly prone to error, Perrine conducted his research using rapid photographic dry plates.

The observations took place during the 1901 eclipse in Sumatra, carried out by the Crocker Expedition of the Lick Observatory [70]; the remarkably long totality phase (6 minutes and 30 seconds) was particularly conducive to the search for an intra-Mercurial planet. Despite adverse weather conditions, the results were highly detailed: across six different observation areas, a total of 170 star images were recorded. In the first two sets of exposures, stars with a visual magnitude between 8.7 and 9.3 were captured, while, during the final stages of the eclipse, the clouds became thicker, preventing the capture of stars fainter than magnitude $V = 6.0 - 6.5$. However, the observation remained highly reliable, detecting only two known bright stars in the entire region.

Consequently, Perrine deduced that since the plates recorded stars of these magnitudes, a hypothetical planet of magnitude $V = 7.5 - 8.0$ must have been recorded. Such an object corresponds to a diameter of about D = 48 km (30 miles [70]), just as a brighter magnitude 5.0 planet corresponds to a diameter of roughly 120 km (75 miles) [70]. Therefore, explaining the orbital perturbations of Mercury requires an enormous mass, achievable only by a cluster of about one million of these small planets, assuming a density equal to that of Mercury itself [70]. Perrine thus concluded that there were probably "no bodies of appreciable size" in the region close to the Sun and that the cause of the anomalies in Mercury's orbit might reside in the finely divided matter composing the Zodiacal Light [70].

The definitive presence or absence of these objects serves as a crucial test for planetary formation theories, helping to discriminate between aerodynamic fractionation models and giant impact scenarios [18]. According to Campins et al. [18], past efforts consistently yielded negative results and ruled out only the existence of relatively large bodies, leaving a population of smaller, asteroid-sized objects completely undetected. Depending on the solar phase angle and heliocentric distance, the limiting photographic magnitudes achieved (ranging from $V = 5$ to $V = 9$) strictly constrain only bodies with radii larger than 25 to 160 km, assuming a geometrical albedo equal to that of Mercury $p_V = 0.14$ [18].

To establish more definitive constraints, researchers recognised the need to shift to the infrared spectrum and define clear dynamical boundaries. According to thermodynamical constraints, the stable zone where Vulcanoids could have survived over the age of the Solar System is restricted to a narrow region between 0.1 and 0.25 AU from the Sun [18]. Beyond 0.25 AU, planetary perturbations secularly increase orbital eccentricities, causing objects to overlap with Mercury's orbit and be swept up, while even within the stability zone, these perturbations induce high impact velocities (up to 5 km/s), leading to severe collisional erosion that destroys larger bodies in less than 1 billion years [53] [18]. At the inner edge of 0.1 AU, objects are subject to severe sublimation and Poynting-Robertson drag; under these extreme conditions, the minimum radius required for a body to survive for 4.5 Gy is approximately 1 km [18].

Ground-based infrared searches within this region were initiated between 1979 and 1981 by Leake et al. [53]. Since objects close to the Sun emit significant infrared radiation, they employed a daytime search using a single-detector bolometer on the 1.3-metre telescope at the Kitt Peak National Observatory [53] [18]. To prevent direct sunlight from striking the telescope optics, they utilised a dedicated solar baffle. Observations were conducted in the infrared L band (near a wavelength of 3.5 µm), where the daytime sky background brightness reaches a minimum [53]. Their setup involved performing raster scans over $450'' \times 450''$ areas of the sky, primarily utilising a 22 arcsecond aperture with 2 to 4-second integration times. At the same time, another portion of the search employed a 45-arcsecond aperture [53] [18], achieving a limiting L-band magnitude of 5 (corresponding to a radius of $\sim$ 5 km at 0.2 AU). Later, in 1989, Campins et al. [18] performed a feasibility test using a near-infrared InSb array camera, demonstrating that a limiting magnitude of $L = 6$ could be reached. This sensitivity represents a significant threshold, as it theoretically allows the detection of objects down to the 1 km survival limit (specifically, down to a radius of 0.7 km at 0.1 AU [18]). However, these early infrared campaigns were heavily bottlenecked by the technology of the time: the long readout and data-storage overheads (up to 15 minutes per frame) were incompatible with the expected rapid apparent motion of Vulcanoids, which can reach up to 5 arcmin/hour [18].

4.2 Space-based Searches

The problem of Vulcanoids' proximity to the Sun can be circumvented by observing from space, particularly using images from the SOHO (Solar and Heliospheric Observatory) space telescope, a joint ESA-NASA project launched in 1995 for continuous observation of our star. To evaluate the sensitivity of space-based searches, it is necessary to consider the technical specifications of the Large Angle Spectroscopic Coronagraph (LASCO) suite, particularly the C3 instrument.

LASCO C3 is an external occulted Lyot-type coronagraph designed to image the solar corona in broadband white light [13]. The C3 instrument observes a region extending from 3.7 to 30 solar radii ($R_\odot$), corresponding to approximately 0.02 to 0.14 AU [13], covering a significant portion of the Vulcanoid Zone. The instrument employs a 1024×1024 pixel CCD detector with a relatively coarse spatial resolution of 56 arcseconds/pixel [13]; such a large pixel scale implies that small and faint targets are easily lost within the background noise or confused with cosmic ray hits and star images. Due to the small distance between the external occulting discs and the entrance aperture, the inner portion of the C3 field is significantly vignetted. Furthermore, the brightness of the F-corona [1] and the high levels of stray light near the occulter edge create a high-noise environment, making the detection of low-albedo objects extremely challenging.

In 2000, Durda et al. [32] analysed a continuous 40-day sequence of images (from January 1 to February 9, 1997) from the SOHO/LASCO C3 coronagraph, searching for potential Vulcanoids in heliocentric orbits with radii from 0.07 to 0.21 AU. The choice of a 40-day observation window was not arbitrary but derives from the fact that the synodic period of a body at the outer edge of the VZ (0.21 AU) is 38.87 days. By exceeding this duration, the authors ensured that any Vulcanoid crosses the instrument's field of view (FOV) at least once.

The search was performed by visually blinking daily image averages that had been registered on background stars to identify any moving objects not present in the catalogues. To test the instrument's sensitivity and the effectiveness of the blinking technique, around 50 artificially simulated Vulcanoids with magnitudes ranging from $V = 6.0$ to 9.5 were inserted into the archival images. The reliability of this method was further confirmed by the incidental detection of well-known moving bodies, such as the asteroid 4 Vesta at magnitude 7.7, as well as the planets Uranus and Neptune.

Within the surveyed region, no positive detections were yielded, establishing a moving object detection limiting magnitude of $V = 8.0$. Based on this photometric limit, and assuming a Mercury-like albedo ($p_V = 0.14$), the search ruled out the existence of Vulcanoids larger than 20 km in diameter at the inner boundary (0.07 AU) and

[1] The F-corona, or Fraunhofer corona, is regarded as the inner continuous extension of the zodiacal light at smaller elongations of the line of sight, produced by interplanetary dust particles scattering sunlight and emitting thermal radiation [50].

larger than 60 km at the outer boundary (0.21 AU) [32]. Finally, by extrapolating the results with a collisional equilibrium power-law size distribution, the authors estimated that the entire Vulcanoid population larger than 1 km in diameter is no greater than roughly 1,800 to 42,000 objects [32].

In conclusion, the absence of detections in the SOHO data suggests that if a Vulcanoid population currently exists, it must be composed of objects significantly smaller than the resolution and sensitivity limits of the LASCO C3 instrument. Consequently, the gap in our knowledge remains for objects in the range 1 to 10 km, which requires instruments with higher dynamic range and finer spatial resolution to be identified against the solar glare.

Another important contribution to the understanding of the present-day Vulcanoid population is provided by the collisional evolution models of Stern and Durda [80]. These authors showed that the long-term survival of bodies in the Vulcanoid region depends sensitively on several factors, including orbital eccentricity, heliocentric distance, and the physical strength of the objects. Their simulations indicate that collisional grinding is extremely efficient in this region, leading to a substantial depletion of any primordial population older than the Solar System. As a consequence, the present-day Vulcanoid population, if it exists, is expected to be a small residual component, with the highest survival probability near the outer edge of the dynamically stable zone (around $\sim$ 0.2 AU), where impact velocities are lower and collisional lifetimes are longer. While order of magnitude estimates suggest that only a limited number of kilometer-sized bodies may survive, these predictions remain strongly model-dependent and sensitive to assumptions on the initial size distribution and material properties.

The challenge of detecting such a severely depleted population was later undertaken by Steffl et al. in 2013 [78]. They conducted a highly sensitive search using archival data from the Heliospheric Imager-1 (HI-1) instrument on the STEREO-A space probe, which, together with STEREO-B, makes up the pair of probes of the Solar TErrestrial RElations Observatory (STEREO) mission, launched by NASA in 2006.

As detailed by Eyles et al. [41], the HI-1 camera's optical axis is intentionally off-pointed from the Sun by 14°, allowing its 20° field of view to scan elongations from 4° to 24°, perfectly framing the core of the Vulcanoid Zone. It is equipped with a complex forward baffle system specifically designed to reject stray light from the solar disc, making it significantly more sensitive than traditional coronagraphs [41]. Although the STEREO mission comprises twin probes (A and B), the authors utilised data exclusively from STEREO-A as it has a more stable pointing than STEREO-B [78].

Over 40 days, from December 2008 to January 2009, the image sequences were processed to remove background interference. The researchers applied a "ring-median" background subtraction to filter out the F-corona (zodiacal light) and the highly dynamic transient events, such as solar wind streams and Coronal Mass Ejections (CMEs) [78]. Similar to the SOHO analysis, the background star field was aligned and subtracted. To rigorously quantify the detection efficiency of their methodology, the authors added 101 synthetic Vulcanoids into the processed image sequences.

Unfortunately, even in this case, the search yielded no Vulcanoid detections. The HI-1 instrument is capable of detecting background stars down to approximately 12-13th visual magnitude in processed images, demonstrating its high photometric sensitivity [41]. However, the dedicated Vulcanoid search carried out with HI-1 resulted in a much more meaningful physical constraint: no Vulcanoids larger than 5.7 km in diameter were detected, assuming an R-band albedo of $p_R = 0.05$ and a Mercury-like phase function. This 3σ (99.7%) statistical confidence limit applies to the entire dynamically stable zone (specifically for orbits with eccentricity $e \leq 0.15$ and inclination $i \leq 15°$) [78]. Furthermore, based on standard asteroid size-frequency distributions, Steffl et al. concluded that there are no more than 76 Vulcanoids larger than 1 km remaining in the inner Solar System [78], confirming that any surviving Vulcanoid population must be exceptionally small.

As Merline and colleagues pointed out in 2016, the delivery of a telescope to the environs of Mercury by the MErcury Surface, Space ENvironment, GEochemsitry, and Ranging (MESSENGER) mission provided an opportunity to search for small bodies near the Sun that are difficult to detect from Earth [57]. The primary instrument used for these surveys was the Wide-Angle Camera (WAC), part of the Mercury Dual Imaging System (MDIS) [57]. Despite its small aperture of just 8 mm, the WAC compensated with a $10.5° \times 10.5°$ field of view and the capability to perform long exposures of up to 10 s using a broadband visible filter, allowing it to capture faint background stars.

However, the search for Vulcanoids faced operational constraints. Due to thermal safety constraints, the spacecraft was prohibited from pointing within 30° of the Sun [57]. This restriction prevented observation of the innermost part of the Vulcanoid Zone, limiting its search area to the outermost 46% of the stable region during its cruise phase, and only 5% once it entered orbit around Mercury [57]. To isolate potential candidates, sequences of consecutive exposures were acquired to filter out cosmic rays and artefacts, and the images were co-added to highlight any orbital motion relative to the background stars.

In addition to the Vulcanoid survey, MESSENGER was positioned to search for hypothetical natural satellites of Mercury [57]. Operating from the spacecraft's apoapsis, the highest point of its eccentric orbit around the planet, the WAC scanned upward relative to the expected equatorial plane. The camera executed incremental "stepping" sequences, moving outward from 2 to 75 Mercury radii (R_M) and then back. This pattern was specifically optimized to dynamically isolate satellites moving at various orbital velocities, ensuring they are tracked before leaving the field of view, covering approximately 20% of the near-equatorial orbital phase space [57].

While the mission did not yield any positive discoveries, the spacecraft's close proximity ensured that any potential targets appear significantly brighter than they would from Earth, enabling exceptionally tight constraints. The campaign ruled out the existence of Vulcanoids larger than $4 - 6.5$ km within the surveyed regions [57]. Furthermore, for Mercury's immediate orbital environment, the search achieved a 90% completeness level, excluding any companion satellites larger than 10 m at close range ($2\,R_M$) and larger than 100 m at the outer boundary ($75\,R_M$) [57].

4.3 Solar Eclipse Campaigns

An alternative to space probes is to search for intra-Mercurial objects during the few minutes of a solar eclipse. This was clear over a century ago during the early expeditions such as Perrine's 1901 campaign [70] discussed in Section 4.1. Following this expedition, Perrine himself carried out subsequent photographic searches during Total Solar Eclipses (TSEs) in 1906 [69] and 1909 [71], Campbell and Trumpler in 1923 [16], and Courten in 1976 [25], all yielding negative results.

TSEs offer an effective window to search for Vulcanoids from Earth because the background sky brightness becomes similar to that about 30 minutes after sunset, and although the sky never becomes completely dark, fainter limiting magnitudes can be reached, enabling the detection of asteroids about 1 km in diameter.

While early attempts relied on the photographic technology of the time, modern campaigns utilise advanced digital sensors, filters, and image-processing techniques. A search for Vulcanoid asteroids was made during the Total Solar Eclipse (TSE) of August 1, 2008, in China by Zhao et al. [95]. The best strategy for Vulcanoids' search is to select two observational sites along the eclipse path; a Vulcanoid recorded by both sites is more easily identified by blinking the images. During 2008 TSE, the two selected sites were Jiuquan and Yiwu, in the west of China [95].

To optimise the detection of Vulcanoids, which are hotter than Mercury and thus favour the red end of the spectrum, the researchers utilised a specific setup. They equipped a 150 mm aperture telescope with a Kodak KAF-1001E CCD and a Schott RG10 filter [95]. This specific filter improved the Signal to Noise Ratio (SNR) by blocking the blue sky background and the green wavelengths of the solar corona [95]. To further avoid coronal glare during totality, the telescopes were aimed at least 2.5° away from the centre of the Sun and restricted within ±2° near the ecliptic plane [95]. The detailed specifications of the observation facilities are summarised in Table 4.1.

Table 4.1: Observation facilities and specifications from Zhao et al. (2009).

Component	**Specification**
Telescope	Aperture $\phi = 150$ mm, Focal length $f = 200$ mm, F/1.33
	Mount: Germany educational
	Telescope FOV: $10° \times 10°$
CCD	Kodak KAF-1001E
	Dimension: 1024×1024 pixels
	Pixel resolution: 24 μm $\times$ 24 μm ($24'' \times 24''$)
	Full capacity (typ.): $200,000$ e$^-$
	QE @ 400 nm: 39%; Peak eff. @ 560 nm: 72%
	CCD FOV: $7° \times 7°$
Filter	Schott RG10

During the eclipse, sequences of 1, 2, 4, and 5-second exposures were taken to map the area [95]. A limiting magnitude of +12.834 (V) or +13.500 (B) was reached at the Yiwu site, while Jiuquan reached +9.27 (V) or +10.735 (B). This discrepancy arose because the sky background brightness at Yiwu was about 7 times dimmer than that at Jiuquan during the event [95]. Unfortunately, no Vulcanoids were detected, which rules out the presence of asteroids larger than $2 - 6$ km in the analysed area [95]. Being so close to the Sun, the solar corona itself contributes to raising the background; furthermore, Vulcanoids located behind our star, or transiting across the solar disc remain undetectable due to their small angular size.

To overcome the limitations of traditional ground-based observations, such as atmospheric seeing, local weather conditions and the limited temporal window of totality, Caspi et al. [21] have explored an intermediate solution between ground telescopes and space missions during the 2017 TSE. They utilised two NASA WB-57 high-altitude research aircraft. By operating in the stratosphere at altitudes around 16.1 km (about 52,900 ft), these mobile airborne platforms fly above most of the Earth's atmospheric air mass and water vapour, mitigating seeing effects and infrared absorption [21]. Furthermore, flying along the eclipse path in tandem allowed them to significantly extend the duration of totality to over 7 minutes compared to a stationary observer.

The WB-57 aircraft were equipped with the Airborne Imaging and Recording System (AIRS), a two-axis stabilised pointing platform mounted in the nose cone [21]. This mount hosted the DyNAMITE (Day/Night Airborne Motion Imagery for Terrestrial Environments) instrument suite, including both a visible-light camera and a mid-wave infrared (MWIR) scientific camera [21]. To improve the contrast of hot coronal loops against the background, the visible channel utilised a narrowband green filter centered at 533.9 nm to isolate the Fe XIV coronal emission line (the so-called "coronium") [21]. The detailed specifications of this airborne setup are summarised in Table 4.2.

Table 4.2: Observation facilities and specifications from Caspi et al. (2020) [21].

Component	Specification
Platform & Mount	NASA WB-57F aircraft (altitude: 16.1 km)
	AIRS (two-axis stabilized pointing platform in the nose cone)
Visible Camera	HD broadcast television camera, 3-channel CCD (RGB)
	Dimension: 1920×1080 pixels
	Optics: ~ 220 mm aperture, F/1.6, FOV: $1.6° \times 0.9°$
	Filter: Green centered at 533.90 ± 4.75 nm (FWHM ~ 9.5 nm)
	Exposure: ~ 30 ms at 30 Hz
MWIR Camera	Scientific camera with actively cooled InSb detector
	Dimension: 1344×784 pixels
	Optics: ~ 220 mm aperture, FOV: $1.2° \times 0.7°$
	Bandpass: $3 - 5$ μm
	Exposure: ~ 30 ms at 30 Hz

It is important to clarify that Caspi's 2017 expedition was not specifically designed to search for Vulcanoids, instead, the primary goal was to test the feasibility of this high-altitude airborne platform and to investigate the dynamics and thermal structure of the solar corona. An example of the coronal imaging achieved during this mission is shown in Figure 4.1.

Nevertheless, this airborne methodology effectively acts as a bridge, combining the agility, serviceability, and payload capacity of ground observations with the viewing conditions comparable to space-based observatories [21].

4.4 Estimate of the SNR for Vulcanoid Search during Eclipse

This section summarizes the mathematical model used to estimate the signal-to-noise ratio (SNR) of the brightest pixel produced by a point source observed with a digital detector during short-exposure imaging. The formulation assumes a Gaussian point spread function (PSF) and includes photon noise from the source, sky background noise, and detector read noise. Note that this model estimates the SNR of the single brightest pixel rather than the total SNR obtained by aperture photometry. For

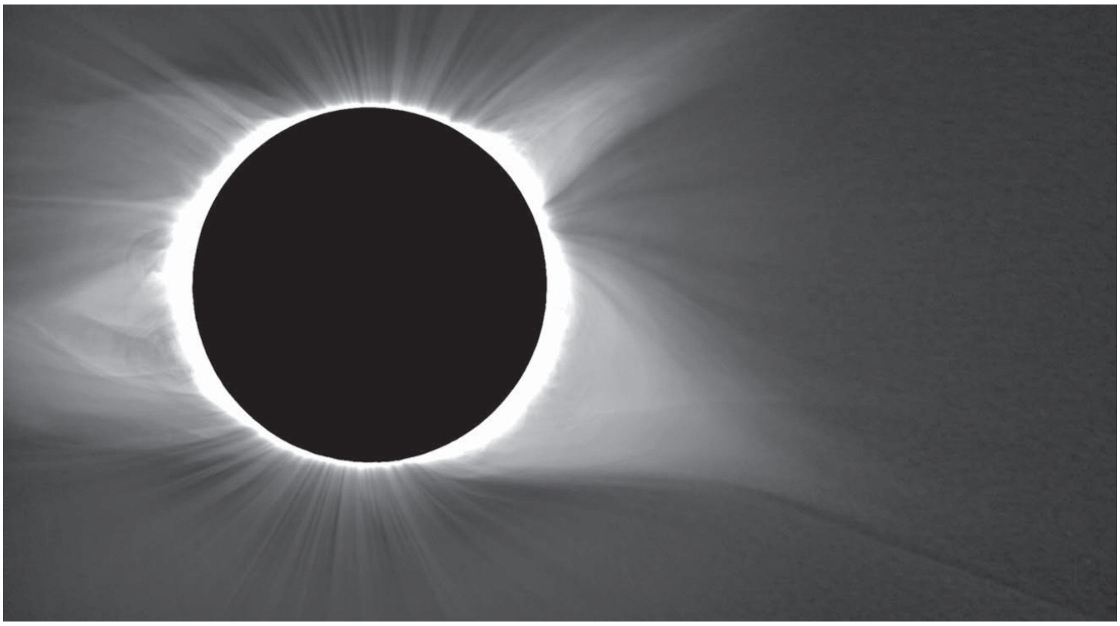

Figure 4.1: Image of the solar corona captured during the 2017 total solar eclipse by the AIRS instrument suite on the NASA WB-57 aircraft. Expeditions like this demonstrate the potential of mobile platforms for coronal studies (adapted from Caspi et al., 2020 [21]).

moving-object searches using shift-and-stack techniques, the effective detection SNR can be higher because the signal from multiple pixels and multiple frames is combined along the expected motion vector. The model neglects detector cosmetic defects, imperfect flat-fielding, variable atmospheric transparency, and tracking errors. Therefore, it represents an optimistic estimate of the achievable limiting magnitude.

4.4.1 Analytical Formulation of the Model

To construct the final SNR equation, it is first necessary to quantify all the physical, instrumental, and observational parameters, including the target and background fluxes, the detector geometry, and the noise contributions. These components are defined as follows:

Photon flux from the target

Equation:

$$F^* = F_0 \cdot 10^{-0.4m} \tag{4.1}$$

Where:
F^*: photon flux from the target star (photons s^{-1} m^{-2})
F_0: photon flux of a zero-magnitude star integrated over $400 - 700$ nm (approx. 4×10^{10} photons s^{-1} m^{-2})
m: apparent magnitude of the target

Sky background photon flux

Equation:

$$F_{\text{sky}} = F_0 \cdot 10^{-0.4\mu} \tag{4.2}$$

Where:
F_{sky}: photon flux from the sky background per square arcsecond (photons s^{-1} m^{-2} arcsec^{-2})
μ: sky surface brightness in magnitudes per square arcsecond (mag arcsec^{-2})

Signal in the brightest pixel

Equation:

$$S_{\text{peak}} = F^{*} \cdot A \cdot QE \cdot t \cdot f_{\text{pixel}} \tag{4.3}$$

Where:
S_{peak}: number of detected electrons in the brightest pixel
A: telescope collecting area (m^2)
QE: total system quantum efficiency (optics transmission × detector QE)
t: exposure time (seconds)
f_{pixel}: fraction of the total PSF flux falling inside the brightest pixel (depends on seeing and pixel scale)

Sky background electrons in one pixel

Equation:

$$B_{\text{pix}} = F_{\text{sky}} \times A \times QE \times t \times \Omega_{\text{pix}} \tag{4.4}$$

Where:
B_{pix}: sky background electrons accumulated in one pixel
Ω_{pix}: angular area of one pixel on the sky (arcsec^2)

Pixel-scale relation:

$$s = 206265 \times \frac{p}{f} \tag{4.5}$$

Where:
s: pixel scale (arcsec/pixel)
p: pixel size (metres)
f: focal length (metres)

Pixel area on the sky:

$$\Omega_{\text{pix}} = s^2 \tag{4.6}$$

This term converts the surface brightness of the eclipse sky into the number of background electrons recorded by a single detector pixel during one exposure.

Noise model

Equation:

$$\sigma = \sqrt{S_{\text{peak}} + B_{\text{pix}} + RN^2} \tag{4.7}$$

Where:
σ: total noise in the brightest pixel (electrons)
B_{pix}: number of background electrons from the sky in the pixel
RN: detector read noise per pixel (electrons RMS)

Signal-to-Noise Ratio

Equation:

$$\mathrm{SNR} = \frac{S_{\mathrm{peak}}}{\sigma} \tag{4.8}$$

The SNR expresses how strong the signal of the target is relative to the total noise that affects the pixel measurement. For faint-object detection, typical detection thresholds range from SNR ≈ 3 (marginal detection) to SNR ≈ 5 (reliable detection).

4.4.2 Numerical example: 135 mm lens + ASI2600MM

Assumed setup and observing conditions as follow:
Focal length $f = 135$ mm $= 0.135$ m
Optical speed $f/2 \to$ aperture diameter $D = 135/2 = 67.5$ mm $= 0.0675$ m
Pixel size $p = 3.76\ \mu$m $= 3.76 \times 10^{-6}$ m (ZWO ASI 2600 MM)
Total $QE = 0.65$
Zero-magnitude flux $F_0 = 4 \times 10^{10}$ photons s^{-1} m^{-2}
Sky brightness $\mu = 13.5$ mag arcsec^{-2}
Read noise $RN = 1.5$ e^{-}
Target magnitude $m = 13.5$
Seeing FWHM $= 6.0$ arcsec
Exposure time $t = 0.2$ s

Step 1 - Telescope collecting area:

$$A = \pi \left(\frac{D}{2}\right)^2 = \pi \left(\frac{0.0675}{2}\right)^2 \approx 3.58 \times 10^{-3}\ \mathrm{m}^2 \tag{4.9}$$

Step 2 - Pixel scale:

$$s = 206265 \times \frac{p}{f} = 206265 \times \frac{3.76 \times 10^{-6}}{0.135} \approx 5.74\ \mathrm{arcsec/pixel} \tag{4.10}$$

Step 3 - Pixel angular area:

$$\Omega_{\mathrm{pix}} = s^2 \approx (5.74)^2 \approx 32.95\ \mathrm{arcsec}^2 \tag{4.11}$$

Step 4 - Target photon flux:

$$F^* = 4 \times 10^{10} \times 10^{-0.4 \times 13.5} \approx 1.59 \times 10^5\ \mathrm{photons\ s^{-1}\ m^{-2}} \tag{4.12}$$

Step 5 - Total source electrons collected in one exposure:

$$S_{\mathrm{total}} = F^* \times A \times QE \times t \tag{4.13}$$

$$S_{\mathrm{total}} \approx (1.59 \times 10^5) \times (3.58 \times 10^{-3}) \times 0.65 \times 0.2 \approx 74\ \mathrm{e}^- \tag{4.14}$$

Step 6 - Brightest-pixel signal:

Gaussian sigma from seeing:

$$\sigma_{\mathrm{PSF}} \approx \frac{\mathrm{FWHM}}{2.3548} = \frac{6.0}{2.3548} \approx 2.55 \text{ arcsec} \tag{4.15}$$

The central-pixel fraction is

$$f_{\mathrm{pixel}} = \left[\mathrm{erf}\left(\frac{s}{2\sqrt{2}\sigma}\right)\right]^2 \tag{4.16}$$

$s =$ pixel scale (arcsec/pixel)
For this configuration, a representative central-pixel fraction is $f_{\mathrm{pixel}} \approx 0.55$

$$S_{\mathrm{peak}} = S_{\mathrm{total}} \times f_{\mathrm{pixel}} \approx 74 \times 0.55 \approx 41 \text{ e}^- \tag{4.17}$$

Step 7 - Sky background flux per arcsec^2:

$$F_{\mathrm{sky}} = 4 \times 10^{10} \times 10^{-0.4\times 13.5} \approx 1.59 \times 10^5 \text{ photons s}^{-1} \text{ m}^{-2} \text{ arcsec}^{-2} \tag{4.18}$$

Step 8 - Sky electrons in one pixel:

$$B_{\mathrm{pix}} = F_{\mathrm{sky}} \times A \times QE \times t \times \Omega_{\mathrm{pix}} \tag{4.19}$$

$$B_{\mathrm{pix}} \approx (1.59 \times 10^5) \times (3.58 \times 10^{-3}) \times 0.65 \times 0.2 \times 32.95 \approx 2.438 \times 10^3 \text{ e}^- \tag{4.20}$$

Step 9 - Total noise:

$$\sigma = \sqrt{S_{\mathrm{peak}} + B_{\mathrm{pix}} + RN^2} \tag{4.21}$$

$$\sigma \approx \sqrt{41 + 2438 + 1.5^2} \approx \sqrt{2481.25} \approx 49.8 \text{ e}^- \tag{4.22}$$

Step 10 - Brightest-pixel SNR:

$$\mathrm{SNR} = \frac{S_{\mathrm{peak}}}{\sigma} \approx \frac{41}{49.8} \approx 0.82 \tag{4.23}$$

In a single 0.2 s exposure, the brightest-pixel SNR is approximately 0.82 because the observation is strongly background-limited under eclipse conditions. This is expected. Detection of a faint moving object therefore relies on combining many frames with shift-and-add or track-and-stack methods, rather than on the significance of a single pixel in a single frame.

4.5 Empirical Twilight Calibration and Eclipse Background Modeling

To properly constrain the minimum detectable physical diameter of potential intra-Mercurial Vulcanoid asteroids, the local sky background brightness during a Total Solar Eclipse (TSE) must be precisely understood. During the totality phase, the sky is never completely dark due to the intense contribution of the solar corona and peripheral light scattering. Empirical baseline data gathered by Zambri et al. (2013) [93] during the exceptionally long total solar eclipse of July 22, 2009, provides an excellent real-world benchmark for these ambient conditions. Using calibrated Sky Quality Meters (SQM), their team recorded a peak zenith darkness of 16.13 mag/arcsec^2, while the sky near the horizon reached 16.71 mag/arcsec^2. Crucially, at an angular distance of approximately 48° from the eclipsed Sun, the background sky brightness hovered around 15.0 mag/arcsec^2. We have used this measure of the sky background and the similar geometry of the eclipse of July 22, 2009, with that of the eclipse of August 2, 2027, to calibrate a simple sky-background model that accounts for coronal brightness, aerosol, and Rayleigh scattering. The resulting sky background as a function of solar angular distance is shown in Figure 4.2.

When translating these measurements to the narrow stable Vulcanoid Zone, situated very close to the Sun between an angular separation of 5° and 12°, the diffuse background light increases substantially. This localised brightening is driven by forward scattering through the Earth's atmosphere, dominated by Rayleigh scattering from molecular air components and Mie scattering from suspended aerosols, compounded by the proximity of the inner solar corona. Consequently, the realistic sky background expected in the immediate sub-solar Vulcanoid search area degrades to a value between 12.5 and 13.0 mag/arcsec^2.

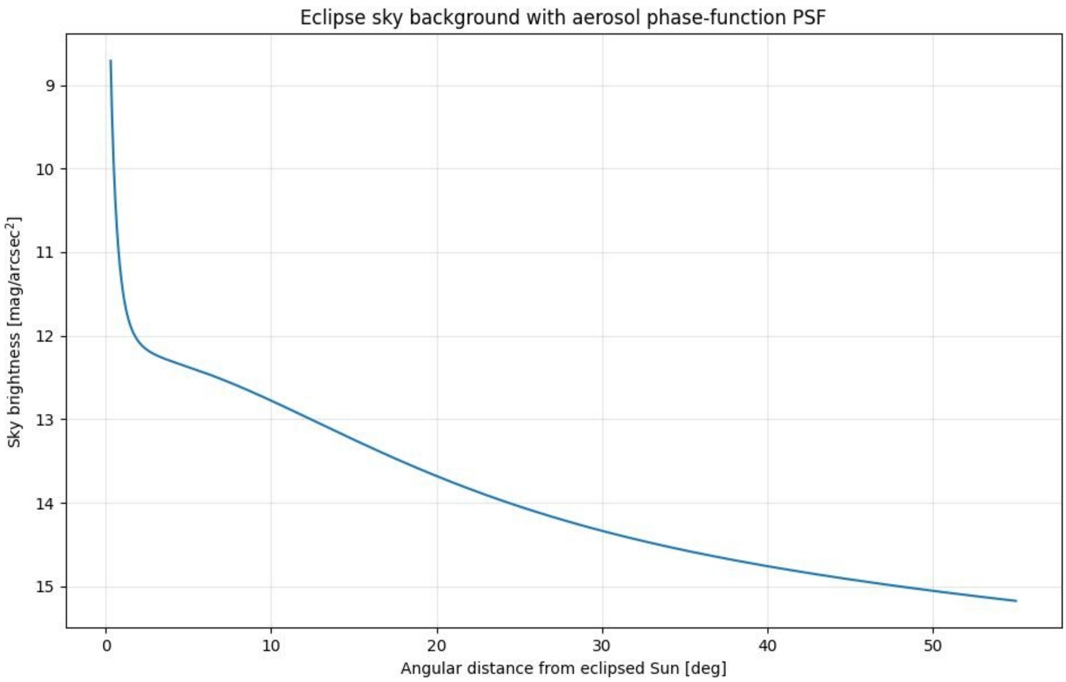

Figure 4.2: Eclipse sky-background model with coronal brightness profile, aerosol, and Rayleigh atmospheric scattering calibrated with [93] vs Sun angular distance for the August 2, 2027 solar eclipse. The observer position is located on the central path of the umbra.

To determine the exact instrumental limiting magnitude under these specific sky conditions, an empirical calibration campaign was executed, utilising twilight illumination to reproduce eclipse sky conditions. The experimental setup consisted of a Samyang 135 mm F/2 telephoto lens mated to a ZWO ASI178MM CMOS camera. To optimise stellar detections, a Minus Violet filter was integrated into the optical train to actively suppress the blue portion of the scattered solar spectrum, thereby artificially darkening the background sky.

The resulting empirical calibration relations are shown in Figure 4.3.

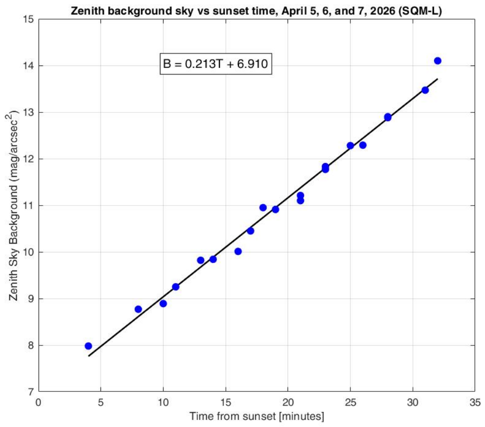

(a) Zenith sky background brightness as a function of the time elapsed from geometric sunset.

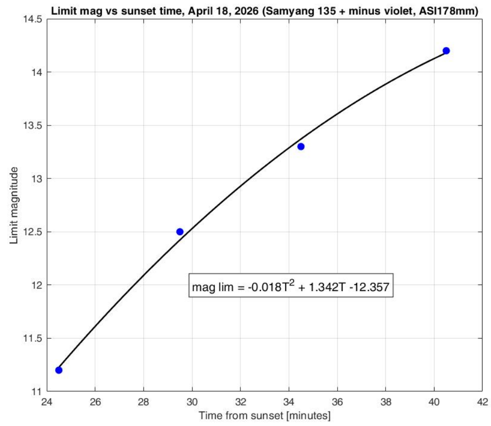

(b) Instrumental limiting magnitude as a function of time elapsed from geometric sunset.

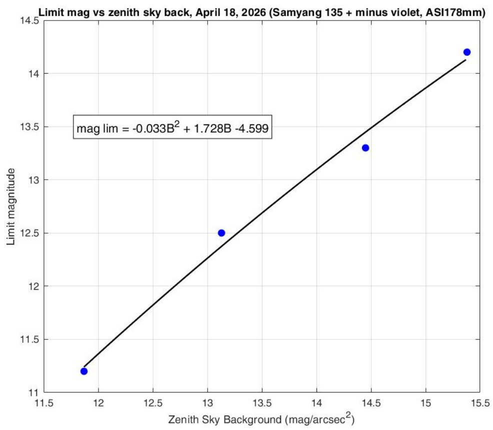

(c) Limiting magnitude correlated with the zenith sky background brightness.

Figure 4.3: Empirical calibrations used to simulate Total Solar Eclipse observing conditions during post-sunset twilight. Data were acquired using a Samyang 135 mm F/2 lens, a ZWO ASI178MM detector, and a Minus Violet filter. Limiting magnitudes were estimated at a detection threshold of SNR $\approx 3-4$ using the UCAC4 stellar catalog. The results show that an eclipse-equivalent sky background ($12.5-13.0$ mag/arcsec^2) yields a limiting magnitude between +11.8 and +12.2 mag, reaching up to +14.2 mag under deeper twilight conditions (40 min post-sunset).

The twilight sky brightness decay was mapped over time along with the corresponding limiting magnitudes of the faintest point sources (extracted at a marginal detection threshold of SNR $\approx 3-4$ and cross-referenced against the UCAC4 astrometric stellar catalogue).

As shown in Figure 4.3a, the target eclipse-equivalent background level of $12.5-13.0$ mag/arcsec^2 corresponds precisely to the twilight window that occurs between

25 and 29 minutes after geometric sunset. Within this narrow operational threshold, the current experimental setup demonstrates a limiting magnitude capability ranging from +11.8 to +12.2 mag (Figure 4.3c). As twilight progresses further to 40 minutes post-sunset, the sky background drops significantly, enabling the setup to achieve a limiting magnitude of +14.2 mag (Figure 4.3b).

These preliminary empirical results indicate that while a compact, wide-field setup can successfully capture stars down to magnitude +12 under simulated eclipse conditions, further optimisations are mandatory to push the detection threshold lower. To detect sub-kilometer Vulcanoids, the background noise must be suppressed by at least an additional magnitude. This can be realistically achieved by swapping the Minus Violet filter for a dedicated IR-Pass filter, which exploits the sharp drop-off of atmospheric scattering at longer wavelengths. Ultimately, developing a comprehensive mathematical model that defines sky brightness as a function of angular distance from the solar limb, atmospheric aerosol loading, lunar shadow diameter, and observer tracking geometry remains a core prerequisite for maximising the efficiency of upcoming eclipse search expeditions.

Chapter 5

Preliminary Search for Vulcanoids during the August 12, 2026, Eclipse

The Total Solar Eclipse (TSE) of August 12, 2026, presents a unique set of geometric and temporal characteristics. The moment of greatest eclipse, defined as the instant when the axis of the Moon's shadow cone passes closest to Earth's centre, will occur on 2026 Aug 12 at 17:47:06 TD [1] (17:45:53 UT1 [2]). This is 2.3 days after the Moon reaches the perigee [37]. During the eclipse, the Sun is in the constellation Leo. The synodic month in which the eclipse takes place has a Brown Lunation Number [12] of 1282, which is a standardised sequential count of lunar cycles starting from the first new Moon of 1923. The eclipse belongs to Saros series 126 and is the 48th of 72 eclipses in that series. The Saros is a cycle of 223 synodic months (approximately 18 years, 11 days, and 8 hours [38]) that produces nearly identical eclipses, a periodicity already known to ancient Babylonian astronomers [11]. All eclipses in this series occur at the Moon's descending node. The Moon moves northward with respect to the node with each succeeding eclipse in the series and gamma, the distance of the Moon's shadow axis from Earth's centre, increases [37].

Within the context of this specific event, the search for Vulcanoids requires extremely rigorous instrumental and methodological preparation due to the short duration of the observational window and the extreme lighting conditions. For our research goals, the TSE of August 12, 2026, represents a fundamental preliminary campaign ahead of the main event of August 2, 2027.

Given these tight temporal constraints, testing the entire instrumentation in the field is crucial to validate the alignment, tracking, and automated acquisition procedures. Although preliminary tests conducted in the twilight sky offer a good approximation to evaluate the sensor response to twilight sky brightness gradients, only a test during an actual total eclipse allows for an accurate measurement of the impact of the scattered light from the solar corona and the calibration of photometric models. To achieve this, the identification of the optimal observing site along the eclipse path is a crucial first step. Since the totality lasts only a couple of minutes, even partial cloud

[1] TD is the Terrestrial Dynamical Time, the modern astronomical time standard defined by the International Astronomical Union, used for time-measurements of astronomical observations made from the surface of Earth; it is a uniform time scale free of the irregularities of mean solar time.

[2] UT1 is the Universal Time, a time scale based on the rotation of Earth in relation to distant celestial objects (stars and quasars); UT1 is a non-uniform time scale because Earth's rotational period is slowly increasing due to tidal interaction with the Moon.

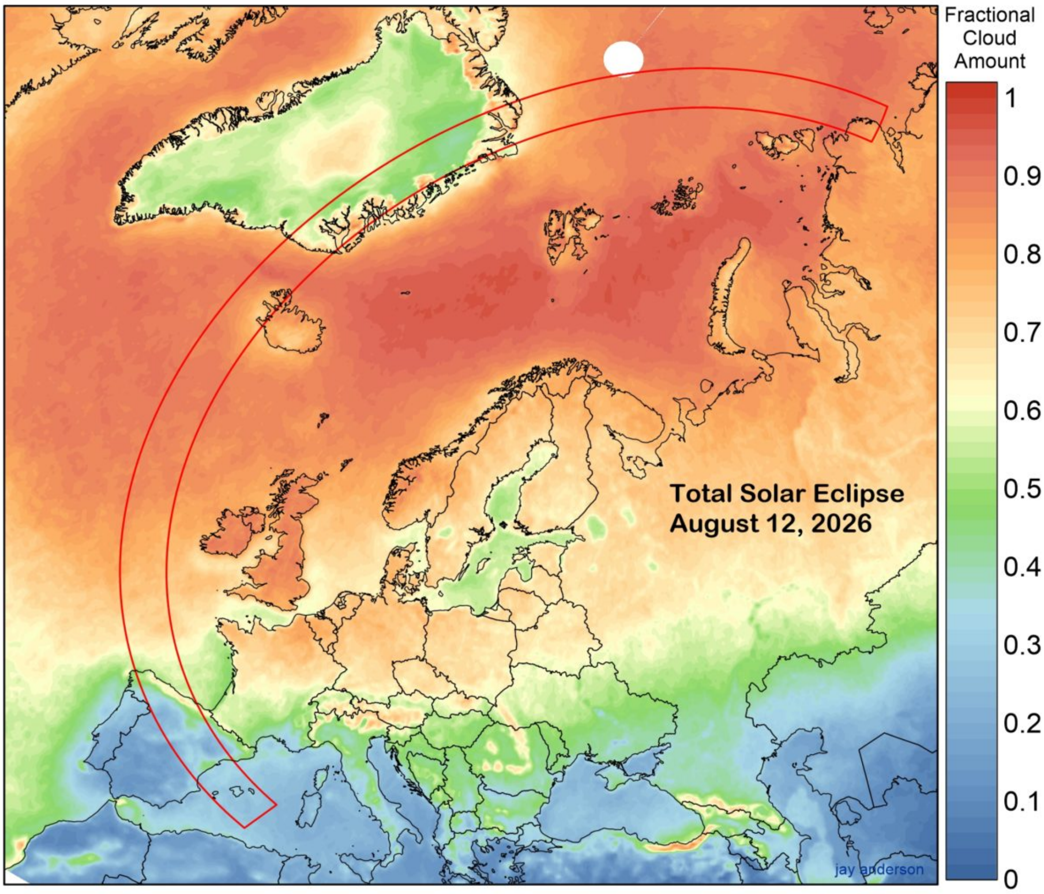

Figure 5.1: Polar-satellite-derived cloud-cover estimates for August based on observations collected between 2001 and 2021. Data: CM SAF/EUMETSAT.

coverage or unfavourable atmospheric conditions could compromise the entire test. For this reason, a detailed study of historical climate data, including cloud coverage, sunshine percentage, precipitation rates, and atmospheric transparency, constitutes an essential component of the preparation process.

5.1 Climatological Analysis and Site Selection

This eclipse will be born and rise in cloud but comes to end of its hours in a sunny and promising Iberian climate. The totality band will touch Artic, Greenland, Iceland and Spain. As shown in Figure 5.1 from Jay Anderson [3], ship-borne viewing sites will be challenged to find good weather; consequently, the best observing sites are on land or close to land. Thus, the choice of the observational site for the 2026 campaign was guided by a careful comparative analysis between the two main landmasses crossed by the path of totality: Iceland and Spain.

Although Iceland offers the geometric advantage of a higher Sun above the horizon between 24° and 26°, its oceanic climate presents an unacceptably high meteorological risk as cloud cover. According to satellite observations, cloud cover averages about 70 to 80% generally across the island compared to the $80 - 90\%$ offshore [3]. Cloud cover over the land has a different character compared to that over water. While over-water cloud tends to come in large broken to overcast sheets, cloud on land is more convective, broken up by the flow over the terrain and by the heating of the land in the daytime. Local weather patterns are also heavily dictated by the prevailing winds. Air piles cloud up on the windward sides of the island and opens skies on the leeward side. Classically, one or more of the several peninsulas that extend into the eclipse zone will have dense cloud on their upwind side and nearly clear skies on their lee [3].

On the other hand, the summer climate of mainland Spain is predominantly sunny. Along most of the eclipse track, the percentage of possible sunshine in August generally exceeds 70%. However, this high probability of clear skies is not uniformly distributed; the complex topography of the peninsula makes certain localised areas more susceptible to cloud formation than others. A comprehensive breakdown of the meteorological and logistical characteristics for the primary candidate locations in Spain is provided in Table 5.1.

Table 5.1: Surface climate observations for sites in Spain. Data taken from Eclipsophile [3].

August climate statistics from ground observations along the eclipse track							
Location	Percent of possible sunshine	Average High (°C)	Highest	Average Low (°C)	Lowest	Pcpn (mm)	Days with rain or snow
Spain							
A Coruña*	56	22.8	39.6	16.4	9.4	35	6
Oviedo*	41	23.3	35.6	14.8	8.6	56	8
Bilbao*	41	26	41.9	15.7	6.8	76	12
Leon*	76	26.9	38.2	12.3	2.6	23	3
Burgos*	68	27.5	38.8	11.5	0.8	23	3.4
Valladolid*	78	30.1	39.5	14.1	3.6	16	2
Logroño*	67	29.8	40.6	15.6	6.2	26	
Soria*	73	28.3	37.4	12.2	1	30	4
Madrid	78	31.3	40.6	18.8	9.2	10	2
Zaragoza*	73	31.7	42.8	18.3	8.4	16.6	2.3
Cuenca*	77	30.7	39.7	15.6	4.8	20	3
Valencia*	68	30.2	43	21.9	16.2	20	2.4
Tarragona*	63	29.4	38	19.7	10.8	42	4
Ibiza*	72	30.3	36.6	22.2	16.5	18	2
Palma*	74	29.8	37.8	22.5	15.8	22	2
Barcelona	66	28.5		20.2		62	5
* indicates that site lies beneath the eclipse umbral shadow. Madrid's NE borders also experience totality.							

Initially, the Balearic Islands (Menorca, Mallorca, and Ibiza) were considered due to their excellent weather prospects, but they were immediately ruled out because the Sun would be extremely low on the horizon there, at an altitude of only about $2^\circ - 3^\circ$. Therefore, the Spanish mainland was chosen, characterised in August by a dry continental climate and a very high probability of clear skies. However, this choice imposes significant observational challenges: in Spain, the eclipse will occur in the late afternoon, shortly before sunset, with the Sun at an altitude ranging from about

10° on the northern coast to just 4° at the Balearic Sea during totality. This geometry entails a higher air mass (X) along the line of sight and, consequently, strong atmospheric extinction. It will therefore be fundamental to evaluate how this atmospheric density affects the contrast between the solar corona and the surrounding sky background, a critical parameter for detecting faint objects. According to the climate analysis by Anderson [3], the geographical profile of the Iberian Peninsula along the 2026 eclipse track is highly diverse, featuring a complex succession of coastal plains, river basins, elevated plateaus, and prominent mountain systems. In the northern region, the Cordillera Cantábrica acts as a crucial meteorological shield. This mountain range traps oceanic moisture originating from the Bay of Biscay along the northern coast, largely preventing humid air masses from penetrating the interior. Although some topographical gaps exist, most notably the corridor between Bilbao and Burgos near the northern edge of the centerline, the terrain's natural elevation (averaging around 1,000 metres) effectively mitigates the inland spread of this moisture.

As the path of totality advances into central Spain, the landscape grows more intricate. North of the eclipse centerline, the shadow will sweep across the lower elevations of the Ebro River Basin. Conversely, the southern portion of the track crosses the Meseta Central, a vast inland plateau with an average altitude of 600 to 700 metres. This plateau is geographically bisected into northern and southern halves by the Sierra de Guadarrama, a mountain range located north of Madrid whose peaks reach up to 2,400 metres above sea level.

Further east, the Sistema Ibérico heavily influences the local topography, starting southeast of Burgos and curving southwards. This extensive network of massive and smaller mountain ranges initially borders the northern edge of the eclipse track before expanding across the southern side as it nears the Mediterranean Sea. Functioning as a major natural divide, the Sistema Ibérico (with modest peaks around 2,300 metres) isolates the central Meseta from both the eastern coastal lowlands and the Ebro Valley.

5.1.1 Cloud and Weather in Spain

The complex topography of the Iberian Peninsula directly dictates its cloud climatology, creating distinct microclimates along the path of totality. As illustrated by the satellite-derived cloud mapping in Figure 5.2, the terrain's elevation profile acts as a primary driver for cloud formation. Higher cloud concentrations (indicated by yellow tones) strictly follow the mountainous elevations, while the lower basins of the Meseta Central and the Ebro Valley benefit from significantly clearer skies (indicated by blue tones).

According to climatological analyses based on two decades of satellite imagery [3], the northern and northwestern maritime fringes represent the highest meteorological risk. This region is continuously exposed to marine moisture. Northerly winds push stratus and stratocumulus clouds onshore, where they are forced upward by the Cordillera Cantábrica. This orographic lift, occasionally combined with Atlantic cold fronts, maintains an average cloud cover of approximately 60%. Consequently, historical data show that early August days in this coastal strip (e.g., near A Coruña or Bilbao) experience cloudy or overcast conditions more than half the time, accompanied by cooler temperatures and higher precipitation rates. However, once the eclipse track crosses the Cordillera Cantábrica and moves inland, the meteorological prospects

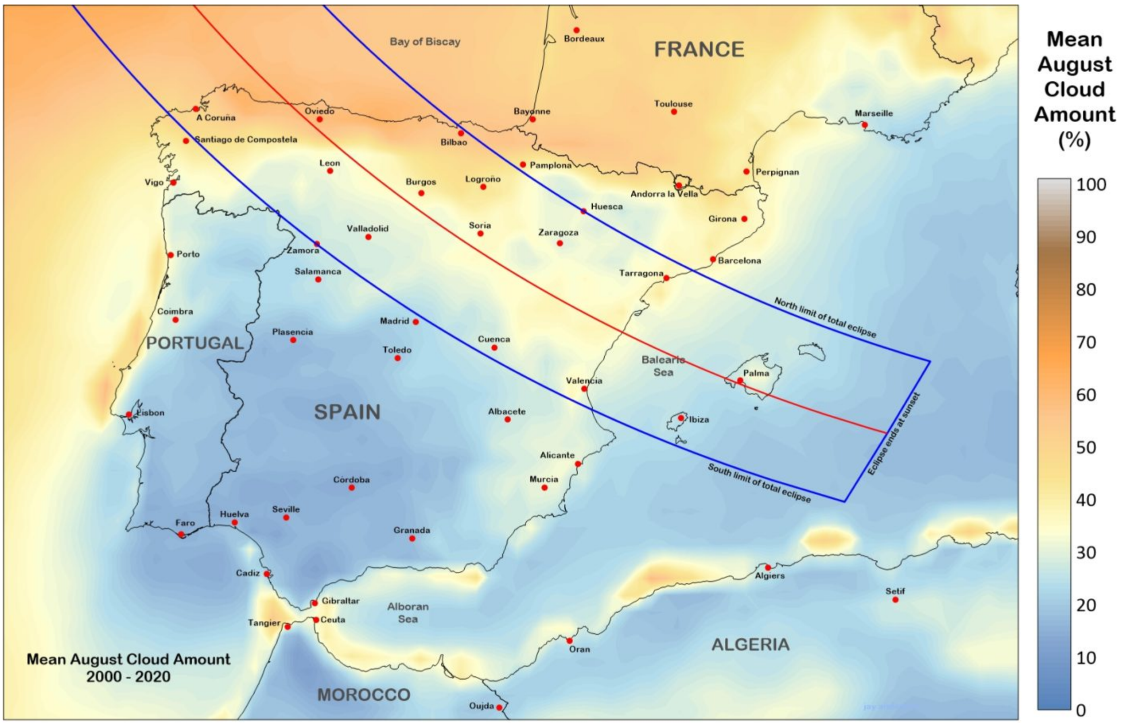

Figure 5.2: Average August cloud cover as measured from polar-orbiting satellites between 2002 and 2020. Data: CM SAF/EUMETSAT.

improve dramatically. In the vast inland plains of the Meseta Central, average cloud cover drops significantly, stabilising around 35%. The northern basin of the Meseta, which includes provinces such as León, Burgos, and Valladolid, boasts some of the highest sunshine percentages on the peninsula, ranging from 68% to 78%. Satellite records indicate a high probability of clear skies in these inland basins, making them statistically optimal for astronomical observations.

Topography continues to play a disruptive role even in the arid interior. Mountainous regions such as the Sistema Ibérico and the Sierra de Guadarrama are covered by dark, low-albedo forests. During the hot Spanish summer, these forests absorb intense solar radiation, rapidly warming the lower atmosphere. If the air mass is sufficiently unstable, this localised heating triggers the formation of convective clouds and afternoon thunderstorms over the peaks. While these mountain ranges impose only a modest statistical penalty on average cloudiness (often less than a 10% increase compared to the plains), their rugged terrain and thick vegetation make it practically difficult to secure an unobstructed view of the low western horizon required for this specific eclipse.

Further east, the Ebro River basin (around Zaragoza) offers exceptionally clear skies, often dropping below 30% cloud cover. However, sites closer to the Mediterranean coast and the Balearic Islands face a different set of challenges. While the coastal cloud cover is generally low, the proximity to the sea fuels afternoon convective clouds. Furthermore, observing from the extreme eastern edges or the islands means the Sun will be at a critically low altitude (barely 2° to 3° above the horizon). While mathematically possible and aesthetically spectacular, observing through such a massive column of dense marine air significantly increases the risk of extinction and atmospheric distortion.

In conclusion, this macro-regional analysis indicates that the inland plains of the

Meseta Central, encompassing cities like León, Burgos, and Valladolid, provide the safest and most stable atmospheric conditions, effectively balancing the need for clear skies with an acceptable solar altitude during totality.

Nevertheless, some meteorological risks remain unavoidable. Summer weather in Spain is frequently influenced by convective activity, and localised thunderstorms can rapidly develop even under otherwise favourable climatological conditions. In extreme cases, such as on August 12, 2025, the convective cloud coverage was so extensive that, had the eclipse occurred then, observations from Spain would have been highly compromised, leaving the Balearic Islands as the only region with potentially clear skies [3].

5.2 Logistics and Institutional Partnerships

Operating in a foreign country during a major astronomical event requires careful logistical planning, particularly regarding the transportation of delicate and heavy instrumentation. The expedition team will consist of four members tasked with safely transporting a substantial payload of approximately 225 kg of sensitive equipment, including telescopes, mounts, and digital cameras. Handling this heavy payload necessitates renting a dedicated vehicle upon arrival and prioritises sites with straightforward road access from major airports:

- Overland travel (Van/car): a continuous road trip from Italy to Spain covers approximately 1,750 km and requires at least two days of driving across France and Spain. While this option removes any airline weight restrictions for the equipment, the extensive travel time makes it less optimal;

- Air Travel and local transfer (selected route): the most efficient option involves flying directly from Italy to the major international hub of Madrid. Upon arrival, the team and the equipment will be transferred to the observing region in León using either the high-speed train network (RENFE) or a rented vehicle. To bypass standard airline weight limits and avoid the risk to optics, the heavy payload will be sent in advance directly to the basecamp.

A primary criterion for the mission was identifying locations within the path of totality that also host established astronomical institutions, such as planetariums or public observatories, which could offer logistical support, secure observing grounds, and stable power supplies. Initially, the search focused on university observatories, as an academic environment would provide the ideal infrastructure for a scientific setup. However, major university observatories in the region, such as the one in Madrid, fall entirely outside the path of totality or suffer from extremely low solar altitudes. This geographic constraint required shifting the focus toward local astronomical centres, planetariums, and municipal observatories located strictly within the totality centerline.

To optimise the travel route from Italy, a logistical and economic feasibility analysis was conducted. While major international hubs like Madrid or Barcelona offer significantly lower direct flight costs, they require extensive overland travel (e.g., approximately 2.5 hours and 8 hours of driving, respectively, to reach the inland plateau), carrying heavy equipment. Conversely, flying directly into local airports like León or Valladolid minimises driving time but substantially increases flight expenses.

Based on logistic constraints, a comparative analysis of potential sites was conducted:

- **León:** This is the primary option, offering one of the longest durations of totality (1m 44s) with the Sun at 10°; this location is highly strategic. It is located just 15 minutes from the León airport, allowing for rapid deployment. Crucially, the European Space Agency (ESA) [3] has selected León as its primary public observation point in Spain, hosting a major event at the Palacio de Exposiciones in direct collaboration with the Universidad de León [4]. This institutional backing provides an ideal, scientifically relevant environment. The primary contact for a basecamp is the *Asociación Leonesa de Astronomía (ALA)* [5] at the Pedro Duque Observatory, although this is currently pending final confirmation. As a robust alternative, the team is also evaluating a potential collaboration with the *Asociación Astronómica del Bierzo* in conjunction with the aforementioned Universidad de León;

- **Centro Astronómico Tiedra [6] (Valladolid):** located 42 minutes from Valladolid airport and about 1 hour and 20 minutes from León airport. While it can also be reached via a 2.5-hour drive from Madrid (a more cost-effective flight hub), a rental car remains strictly necessary. The centre will host a private event for the eclipse, providing a highly controlled and secure environment, making it a prime candidate for the setup. However, the site will experience 1 m 13 s of totality, with the Sun at an altitude of approximately 9° above the horizon;

- **Secondary Alternatives:** Other locations, such as A Coruña, Valladolid, Zamora, and Castellón, were analyzed but ultimately discarded. Some cities offer institutional anchors (the Planetarium in A Coruña and the Science Museum in Valladolid) and durations exceeding 1m 15s. Valladolid is particularly advantageous due to its immediate proximity to the local airport. Zamora suffers from a shorter totality duration (39 seconds), while Castellón presents an extremely low solar altitude (4.6°), which would dramatically increase atmospheric extinction.

The final selection prioritises the León region, in the Spanish Meseta Central, as it offers the best compromise between eclipse duration, logistical accessibility from Madrid, high-level institutional support, and favourable climatological conditions, including high sunshine percentages and relatively stable weather during August 2026.

5.3 Experimental Setup and Instrumentation

To maximise the chances of success during the brief totality window (1 minute and 44 seconds), the instrumentation will be divided into four separate operational stations, each with a specific scientific and photographic objective.

[3] www.esa.int
[4] https://www.unileon.es/
[5] https://www.astroleon.org/
[6] https://cieloytiedra.com/eclipse-solar-total-12-de-agosto-de-2026/

5.3.1 Magnitude Tests and Environmental Observations

This station is primarily designed to test the limiting magnitude reached during totality and to monitor environmental conditions and sky obscuration.

- Mount and power supply: an HEQ5 equatorial mount will be used. To ensure maximum portability and avoid the excessive weight of an uninterruptible power supply (UPS), power will be supplied by a lightweight and compact 12 V LiFePO4 lithium battery (2.1 A, weighing approximately 4 kg);

- Optics and main sensor: the main setup consists of a Samyang 135 mm f/2 paired with a cooled CMOS camera (model 178 MM or possibly a USB 3.0 ColdMOS), which will provide a FoV of $3° \times 2°$. The use of a cooled sensor is preferred to minimise thermal noise during limiting magnitude tests. As backup alternatives, we will evaluate the use of an ASI 183, an uncooled FLIR/Allied 183, or a QHY183 with FoV of $5.5° \times 3.5°$ and a resolution of 3.6 arcsec/px;

- Secondary instrumentation: a secondary mount (EQ3) will host a Coronado solar. To record environmental context, the station will be equipped with a Canon 700D paired with an APO 80 mm lens mounted on a fixed tripod. A portable SQM (Sky Quality Meter) will also be used to record the sky's brightness decay, which is essential for calibrating sky background models. All lenses will initially be protected by Astrosolar filters;

- Observation strategy: the primary camera will be pointed 10° East of the Sun, capturing a single field to establish the limiting magnitude during maximum obscuration. Currently, the SQM and secondary cameras will continuously monitor the sky brightness decay and environmental context, providing essential calibration data for the sky background models.

5.3.2 High-Resolution Search for Vulcanoids

This is the main high-resolution station, designed to map the regions adjacent to the sun in search of Vulcanoids.

- Mount: an HEQ5 mount (provided by the OAS) powered by a dedicated battery, will be used;

- Optics and main sensor: the primary instrument will be a high-performance Schmidt camera (Baker Schmidt 200 f/3) paired with a high efficiency QHY600 sensor (16-bit BSI model) capable of providing a FoV of $3.4° \times 2.3°$;

- Pointing strategy: a 50 mm Astrosolar filter with an aperture stop will be used for alignment; this will allow us to point at the Sun in complete safety, acquire the reference coordinates, and maintain the axis. Once the filters are removed during totality, an offset of 3-10 degrees will be set (covering a field of view (FoV) of $3° \times 4°$ captured by the QHY600 camera) to search for any minor bodies while avoiding direct glare.

5.3.3 Automated High-Resolution Coronal Imaging

This dedicated station is specifically configured to capture the morphological details of the solar corona, operating fully automatically to avoid manual interference.

- Mount: a robust photographic tripod;
- Optics and sensors: the tripod will support a multi-camera configuration to hold lenses with varying focal lengths (Zenit 1000, 500, 200, and 16 mm) to fully cover the Sun and its extended corona. These lenses will work in tandem with the Sony Alpha 5000 and two full-frame Sony Alpha 3 cameras (Astra 24×36);
- Imaging strategy: cameras will be programmed for automated acquisition and remote triggering to photograph the innermost and outermost regions of the solar corona without the need for manual intervention during the critical seconds of the eclipse.

5.3.4 Wide Field and In-Axis Corona Imaging

This station will focus on wide-field observation to capture the extended solar corona and cover large portions of the Vulcanoid Zone.

- Mount: a Skywatcher EQ5 (OAS) equatorial mount;
- Optics and sensor: the system will be mounted on a special plate capable of supporting 2 or 3 lenses simultaneously. The primary combination designed for this purpose is a fast Canon EF 85 mm f/1.8 lens paired with a Sony Alpha 3 camera;
- Imaging strategy: the purpose of this setup is to keep the Sun centered and take advantage of the short focal length (approximately 100 mm) to achieve an extremely wide field of view (from 16° up to 24° FoV). This focal length, capable of framing between $13 - 38\ R\odot$, is ideal for recording the extent of the solar corona, which will naturally mask the most intense solar rays overlapping our line of sight. An automatic data acquisition system will also be tested at this station to maximise data collection.

To ensure optimal coverage of both the solar corona and the Vulcanoid stability region, the optical configurations for each observing station have been carefully selected. Table 5.2 summarises the primary combinations of cameras and lenses (or telescopes) deployed across the four stations, along with their respective Fields of View (FoV) and spatial resolutions. These setups provide a strategic balance: the short focal lengths deliver the extremely wide-field imaging (up to 24°) required to map the extended corona, while the longer focal lengths provide the high-resolution capabilities (down to 1.29 arcsec/px) strictly necessary for detecting faint, point-like moving objects.

Table 5.2: Summary of the optical configurations, Fields of View (FoV), and spatial resolutions for the cameras and lenses deployed during the observational campaign. Backup or alternative configurations are marked with an asterisk (*).

Camera	**Optics**	**FoV**	**Resolution**
QHY600	Baker Schmidt 200 f/3	$3.4° \times 2.3°$	1.29 arcsec/px
QHY183	Samyang 135 mm f/2	$5.5° \times 3.5°$	3.6 arcsec/px
ASI178MM*	Samyang 135 mm f/2	$3.0° \times 2.0°$	3.6 arcsec/px
Sony Alpha 3	Canon EF 85 mm f/1.8	$24° \times 16°$	14.4 arcsec/px
Canon 700D	APO 80 mm f/4.7	$3.4° \times 2.2°$	2.3 arcsec/px

5.4 Expected Results

Given the specific geometric and atmospheric constraints of the August 12, 2026, Total Solar Eclipse in Spain, the primary objective of this observational campaign is not necessarily the discovery of a Vulcanoid, but rather to serve as a comprehensive preliminary dry run for the upcoming 2027 main expedition.

Specifically, the expected results from this campaign encompass several critical technical and scientific milestones: testing the deployment, alignment, and tracking precision of multiple equatorial mounts under severe time constraints. A key outcome will be confirming the reliability of the automated acquisition system and the precise offset pointing strategies required to safely bypass the direct coronal glare during the brief 1 minute and 44 seconds of totality. Since the eclipsed Sun will be positioned at an extremely low altitude of approximately 10° above the horizon, the line of sight will cross a massive column of dense atmosphere. The campaign is expected to provide fundamental empirical data (via the SQM and the wide-field CMOS detectors) on the actual sky brightness decay, measuring the severe impact of Rayleigh and Mie scattering combined with the low-altitude coronal glow. By analysing the acquired data, we expect to determine the true limiting magnitude and Signal-to-Noise Ratio (SNR) achievable under these specific high air-mass conditions. These measurements will replace the theoretical twilight-based background models with exact eclipse-sky values, allowing us to establish rigorous upper limits on the detectable size of any minor bodies present in the fields of view. Ultimately, the logistical feedback, the assessment of the automated imaging scripts, and the photometric calibration data obtained in León will directly dictate the final instrumental refinements necessary to maximise the efficiency of the main Vulcanoid search planned for the August 2, 2027, eclipse.

Chapter 6

Search for Vulcanoids during the August 2, 2027, Eclipse

The next highly favourable Total Solar Eclipse for Vulcanoid detection near Europe will be on August 2, 2027, with a maximum duration of 6 minutes and 23 seconds. The totality band will pass south of Lampedusa, crossing Morocco, Spain, Algeria, Tunisia, Egypt, Saudi Arabia, Yemen and Somalia.

During the eclipse, the Sun will be in the constellation Cancer. The synodic month in which the eclipse takes place has a Brown Lunation Number [12] of 1294. Furthermore, the eclipse belongs to Saros 136 and is number 38 of 71 eclipses in the series, occurring at the Moon's descending node [36].

Obviously, to highlight the proper motion of Vulcanoids, two locations along the path of totality are needed, observing the same star field, possibly with a field of view of about 10°. Comparing images of the same field of view taken at different times will highlight the proper motion of any Vulcanoids present. For example, considering the centre of the totality band, the maximum eclipse will occur at 08:47 UTC in Tangier (Morocco), at 08:54 UTC in Oran (Algeria), and at 09:11 UTC in Sfax (Tunisia). It is true that the eclipse will reach its maximum duration in Egypt, but the logistics in that area are more complex because it would be necessary to set up two stations in the middle of the desert. As can be seen from Tangier to Sfax, there is a time gap of about 24 minutes, more than enough to highlight the proper motion of potential Vulcanoids, and it would be enough to obtain a preliminary orbital solution.

It is important to emphasize that the realization of this definitive observational campaign during the August 2, 2027, eclipse is strictly contingent upon securing dedicated funding. To this end, a grant proposal has been submitted under the "Curiosity Science" scheme within the INAF *Astrofisica di Frontiera 2025* call.

6.1 Preliminary Climatological Analysis

Although Egypt offers the longest totality, the selection of the observing sites must strictly balance geometrical constraints, logistical feasibility, and, most importantly, weather prospects. A study of the historical cloud coverage for August, shown in Figure 6.1 shows a broad area of blue tones along the track, particularly over Egypt and Libya.

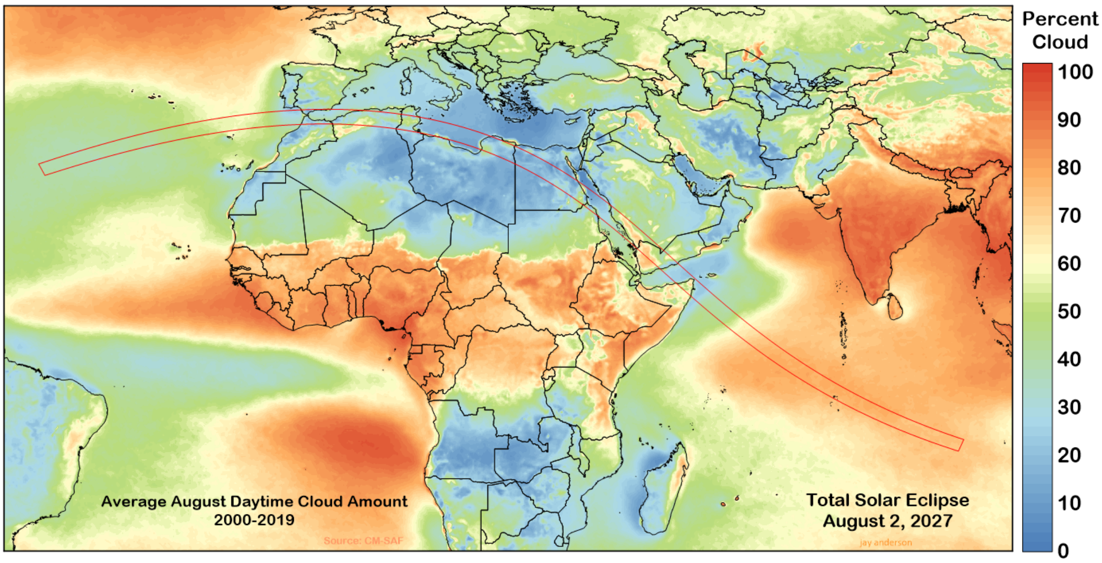

Figure 6.1: Average August cloud fraction from 2000 to 2019 derived from observations by several polar-orbiting satellites throughout the day. Data: EUMETSAT/CM SAF. Eclipse track: Xavier Jubier. Adapted from [2].

Since these data represent daily averages, the variations between morning and afternoon conditions are unresolved [2]. However, a more detailed, time-specific meteorological analysis will be feasible as the date of the eclipse approaches. As illustrated in the map, the path of totality skirts the northern edge of the Sahara Desert. Consequently, locations further east along the track will be heavily characterised by airborne dust, a non-negligible problem since it drastically reduces sky transparency and consequently degrades the expected SNR.

Some parts of the eclipse track, over Libya and western Egypt, have experienced no cloud cover at all in August on eclipse day in the past 23 years. Even in Spain and northwestern Africa, the meteorological prospects are still highly promising [2]. This prevailing good weather along the western and central parts of the track is primarily driven by the Azores (or Bermuda) High, which settles in the mid-Atlantic in midsummer and extends a pressure ridge across northern Spain down into the central Mediterranean near Tunisia [2]. Cloudy disturbances guided by a high-level subtropical jet over Northern Spain can, on rare occasions, reach the African part of the track; a smaller tributary jet stream over Morocco and Algeria can trigger cloud formation and thundershowers when reaching the Atlas Mountains, although these typically develop in the afternoon after the eclipse shadow has passed [2].

Furthermore, the generation of the dust storms mentioned above is heavily influenced by stationary heat lows located in northern Mali and the Arabian Desert, as well as by the Atlas Low in northeast Algeria. As the eclipse track progresses further east, leaving the African continent for the Arabian Peninsula, sunshine prospects begin to weaken. Increasing cloud cover becomes more prominent over the mountains of Arabia, and as the path heads out across the Indian Ocean toward its conclusion near the remote atoll of Diego Garcia [2].

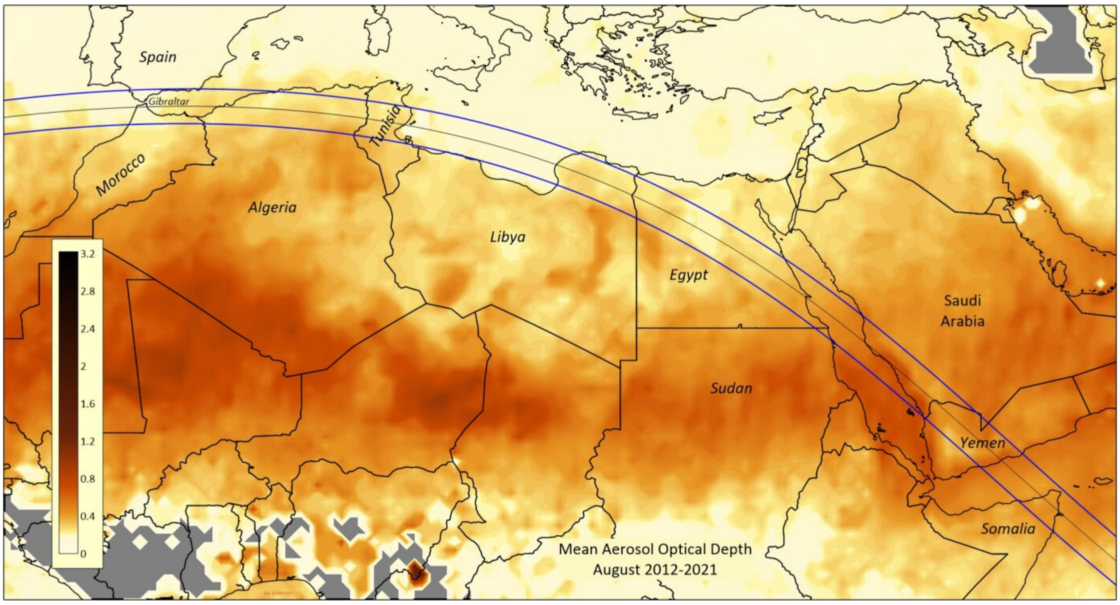

Figure 6.2: Map of average Aerosol Optical Depth (AOD) along the eclipse track derived from daily satellite passes. Data: NASA.

6.1.1 Dust Storms and Sandstorms

It's not possible to plan an observation across the world's largest desert without contending with dust and sandstorms. As illustrated in Figure 6.2 by Jay Anderson [2], the 10-year mean August Aerosol Optical Depth (AOD) over North Africa provides a reliable measure of light extinction caused primarily by suspended dust and haze. For context, an AOD of 0.4 corresponds to a noticeably hazy atmosphere, whereas a value of 1.0 would completely obscure the Sun [2]. Along the eclipse centreline, the average August AOD generally remains around 0.3 until the track passes Luxor, with the lowest and most favourable values recorded near Sfax and Tangier.

From an observer's perspective, most high-altitude dust plumes are semi-transparent, creating a hazy sky that degrades the SNR. Opaque dust storms carrying significant ground-level sand pose a severe risk if an observing site is located close to the source regions, such as the high plateau of Algeria (between the Tell Atlas and Saharan Atlas ranges) or deep within the Sahara Desert. In regions like Spain and Tangier, the primary threat is not ground-level sand, but rather a high-altitude dusty pall blown northward from desert basins in Mali and Mauritania [2].

Further east, in Egypt, dust is surprisingly only an occasional problem during August. Although heavy dust concentrations frequently form over southeast Egypt, satellite images show that these storms tipically retreat before reaching prime observing locations like Luxor [2]. In contrast, the Arabian Peninsula faces the most severe dust conditions along the entire track. Sandwiched between the Arabian Desert and the Sahara, regions such as the Tihamah Plain exhibit the highest average AOD [2], making airborne dust a primary and ongoing concern for any observer stationed there.

6.2 Observational Strategy

An asteroid on a circular orbit between 0.1 and 0.2 AU from the Sun, i.e., in the Vulcanoid's stability zone, will have a maximum elongation seen from Earth from 5.7° to 11.3° (about $11 - 22$ solar radii), and with an orbital speed of 94 and 67 $\mathrm{km\,s^{-1}}$, the maximum angular speed from Earth will be between 8 $\mathrm{arcsec\,min^{-1}}$ to 6 $\mathrm{arcsec\,min^{-1}}$. In 24 minutes, these two hypothetical asteroids will be displaced by 3.2 and 2.4 arcmin, respectively, a quantity that can be easily measured by a modern CMOS detector. If we suppose that these two hypothetical asteroids have a diameter of about 1 km with a geometric albedo of 0.07, the absolute magnitude is about +17.5, and the apparent magnitude from Earth at maximum elongation is between +13 and +14. These are the magnitudes that must be reached in the images to have a nonzero probability of capturing some large Vulcanoids.

During totality, each station will acquire a continuous sequence of short exposures (0.1 s) to maximize the number of usable frames while avoiding saturation. This strategy allows the construction of stacked images optimized for different trial angular velocities corresponding to heliocentric distances within the Vulcanoid stability zone, so we will use the track-and-stack technique used to search for faint near-Earth asteroids.

We will use a commercial wide-field system (described in more detail in the next section), based on a 135 mm $f/2$ lens and a monochrome CMOS detector. We estimate that, adopting eclipse-sky brightness levels consistent with empirical totality measurements and twilight-sky models, the expected 3σ limiting magnitude for a stacked moving-object search is approximately V $\approx 13.5 - 13.7$ per station for about 3 minutes of effective integration on a single field, depending on sky transparency, angular distance from the Sun, and the adopted motion vector. To increase the signal-to-noise ratio, we will use a Schott RG610 filter in front of the lens to eliminate the blue-sky scattering background.

Data reduction will consist of standard calibration (dark/offset calibration, flat-field, bad-pixel mask, coronal background modeled on a large scale), removal of the large-scale background model, and astrometric calibration using background stars visible in the field of view. A dedicated search pipeline based on the shift-and-add (track-and-stack) technique will then combine images according to trial motion vectors between 5 and 10 $\mathrm{arcsec\,min^{-1}}$. Candidate detections will be validated by comparing the predicted position in the image sequence obtained at the second observing site. This cross-validation significantly reduces the probability of false detections caused by cosmic rays, detector artifacts, or transient atmospheric effects. In this way, we can select only bodies with the right characteristics to be real Vulcanoids.

In the months leading up to the eclipse, we will conduct a series of test images of the sky at its zenith, with the Sun at various altitudes below the horizon, using the same setup we will use for the eclipse. This will calibrate an empirical relationship between the sky brightness and the achievable limiting magnitude. The sky brightness during the eclipse is reached approximately 30 minutes after sunset. This will allow us to verify that the magnitude required to detect Vulcanoids approximately 1 km in diameter has been reached. These tests will help select the right exposure time to reach the deepest apparent magnitude and arrive on eclipse day with the right setup.

The proposed experiment requires two identical observing stations located at different positions along the path of totality of the 2 August 2027 total solar eclipse. The two stations will observe the same star field near the Sun with a time separation of approximately $20 - 25$ minutes, allowing the detection of objects moving at angular speeds expected for Vulcanoids ($6 - 8$ arcsec min^{-1}). At the end of the mission, the equipment may remain in use at INAF for educational purposes.

Each observing station will be equipped with a portable wide-field imaging system capable of operating autonomously during the few minutes of totality.

6.3 Wide-Field Optical System

A fast photographic lens with a focal length of 135 mm and an aperture of $f/2$ provides an optimal compromise between field of view and limiting magnitude. Coupled with a modern CMOS detector, the Sony IMX571 with a 23.5×15.7 mm format, this configuration yields a field of view of approximately $10 \times 6.5°$, allowing efficient coverage of the elongation region between about 5° and 12° from the Sun, where Vulcanoids are dynamically stable.

6.3.1 CMOS Detector

A high-sensitivity monochrome CMOS camera, ZWO ASI 2600 MM, is proposed. This sensor is in the APS-C format, which fits very well with the correct field of the Samyang lens, and provides:

- 26 MP resolution (6248×4176 pixels)
- high quantum efficiency ($\sim 90\%$)
- low read noise
- high frame rate capability

These characteristics enable the acquisition of rapid sequences of short exposures (about 1 s) during totality, maximizing the number of frames available for track-and-stack analysis to detect faint moving objects. Based on our simulation, the SNR of the brightest pixel for a hypothetical Vulcanoid of magnitude +14 taken with the 135 mm and the ASI 2600 MM, with a seeing having a FWHM of $3''$, a sky background of 13 mag arcsec^{-2} and an exposure time of 1 s falls within the sensor's non-saturation zone (the FWC of the 2600 MM is 50,000 e^{-}/pixel) with an SNR of 1.65 on the single image, so it would be enough to add at least 100 images to arrive at SNR ≈ 10 and detect the object.

6.4 Mount and Tracking System

A portable harmonic-drive equatorial mount, ZWO AM3, will ensure low mass and accurate tracking without the need for heavy counterweights. Such mounts are particularly suited to eclipse expeditions due to their reliability, compact size, and rapid setup time.

6.4.1 Support Equipment

Each station also requires:

- A portable computer for camera control and data acquisition
- External battery packs, ensuring at least $3 - 4$ hours of autonomous operation
- GPS time synchronization for accurate timestamping of images
- A rigid tripod and protective transport cases for safe transportation of the equipment.

Chapter 7

Conclusions

The quest for Vulcanoids, which originated over 150 years ago, represents one of the most demanding observational challenges in the exploration of our Solar System. It began in 1859 when the French astronomer Urbain Le Verrier, following his success in predicting Neptune's orbit, turned his attention to the anomalous motion of Mercury. He discovered an unexplained excess in the planet's perihelion precession and attributed it to the presence of a new mass or a belt of asteroids closer to the Sun, thus initiating the search for the hypothetical planet Vulcan [4]. Extensive visual and photographic observational campaigns during the solar eclipses culminated in 1909 when W. W. Campbell and C. D. Perrine concluded that no large planetary mass existed with magnitude brighter than $V = 8 - 9$, effectively closing the search [17] [71]. In 1915, Albert Einstein definitively resolved the anomaly by explaining it through his theory of general relativity [35].

Although general relativity removed the necessity for a single massive planet, numerical studies based on Newtonian celestial mechanics demonstrated the existence of a dynamically stable region between approximately 0.09 and 0.21 AU [40] [39] from the Sun. Consequently, the scientific focus shifted to searching for a belt of Vulcanoids, a population of primordial minor bodies. Nevertheless, the definitive existence or absence of a present-day Vulcanoid population has not yet been confirmed primarily due to the severe observational limitations inherent to the extreme inner Solar System where these objects are hypothesised to reside [80] [32] [5]. If a primordial Vulcanoid population did exist, it faced an extremely extreme environment over the 4.5 billion-year history of the Solar System. The high orbital velocities in this intra-Mercurial region lead to highly energetic collisions, meaning that impacts are overwhelmingly erosive and destructive rather than accretional. Furthermore, non-gravitational forces such as the Yarkovsky effect and Poynting-Robertson drag efficiently remove smaller collision fragments (from meters to kilometers in size), causing them to rapidly migrate toward the Sun.

The survival of Vulcanoids is also strictly tied to their composition and the evolution of solar luminosity; as the Sun's luminosity increased over its lifetime, the inner boundary for stability shifted outward due to intense sublimation, especially for rocky or iron bodies. Theoretical models suggest that a regolith layer could potentially act as a thermal buffer, delaying the Yarkovsky drift and significantly prolonging survival times.

However, if any Vulcanoids survive today, they are expected to be extremely rare and limited to only a few kilometres in diameter.

Although dynamical and collisional models suggest that the region has been largely depleted over the age of the Solar System [80, 89], the observational parameter space remains only partially explored. By combining theoretical models with the results of all major observational searches, it is possible to construct a comprehensive detectability map. Figure 7.1 summarises the observational constraints discussed throughout this thesis within a single heliocentric distance-diameter parameter space. The background colour scale and contour lines represent the expected apparent visual magnitude of a hypothetical Vulcanoid as a function of its heliocentric distance and diameter, while the coloured regions indicate the portions of parameter space excluded by previous searches. Objects lying outside these regions remain observationally unconstrained and therefore constitute the primary targets of future observational campaigns. Since the apparent magnitude depends on both diameter and heliocentric distance, bodies of different sizes may exhibit the same apparent brightness if located at different distances from the Sun. To the best of our knowledge, this is the first figure to place all published Vulcanoid observational constraints within a common heliocentric distance-diameter framework.

The proposed solar eclipse campaigns presented in this thesis are specifically designed to probe a critical remaining gap in this parameter space. As illustrated in Figure 7.1, the objective for the 2026 solar eclipse expedition is represented by the purple region, extending from 0.16 to 0.21 AU. This targeted area was strategically selected based on our instrumental constraints and dynamical models. Spatially, we excluded the innermost region because the intense coronal glare and atmospheric scattering increase exponentially closer to the solar limb, and because dynamical models suggest that the outer region represents the most probable "safe zone" where km-scale bodies could have survived the collisional erosion operating near the Sun. In terms of photometric depth, preliminary twilight tests established a limiting magnitude of $V \sim 12.2$ using a Minus Violet filter. However, for the 2026 expedition, we aim to improve this detection limit by optimizing our optical setups and avoiding the use of the Minus Violet filter as detailed in Chapter 5, targeting a deeper limiting magnitude approaching the $V \sim 13.5$.

In constructing this map, a conservative "worst-case scenario" for detection was adopted by assuming a geometric albedo of $p_V = 0.05$, typical of dark C-type asteroids. This represents a realistic observational limit for the survival of Vulcanoid, which could sublimate over the age of the Solar System since an extremely dark body absorbs almost all the incident radiation. To optimise the detection of Vulcanoids outside the solar glare, observations are conventionally targeted at their maximum solar elongation. In this configuration, the geocentric distance of the object is not a fixed parameter but rather a geometric function of its heliocentric distance r, expressed as $\Delta(r) = \sqrt{1 - r^2}$ AU.

The geometric representation of each exclusion zone modeled onto this uniform parameter space reflects its specific detection methodology. The campaign by Durda et al. [32] and Zhao et al. [95], which established apparent magnitude limits of $V = 8.0$ for SOHO and $V = 12.8$ for the 2008 TSE, is represented by curved isolines. Thus, to maintain a constant apparent magnitude as the heliocentric and geocentric distances increase, the physical diameter of the body must also increase, excluding the presence of objects larger than $36 - 106$ km and $3.4 - 10$ km, respectively. Steffl and colleagues [78], instead, established an absolute physical size limit independent of distance; thus, the D$>$ 5.7 km limit set by STEREO/HI-1 across the entire Vulcanoid region is represented

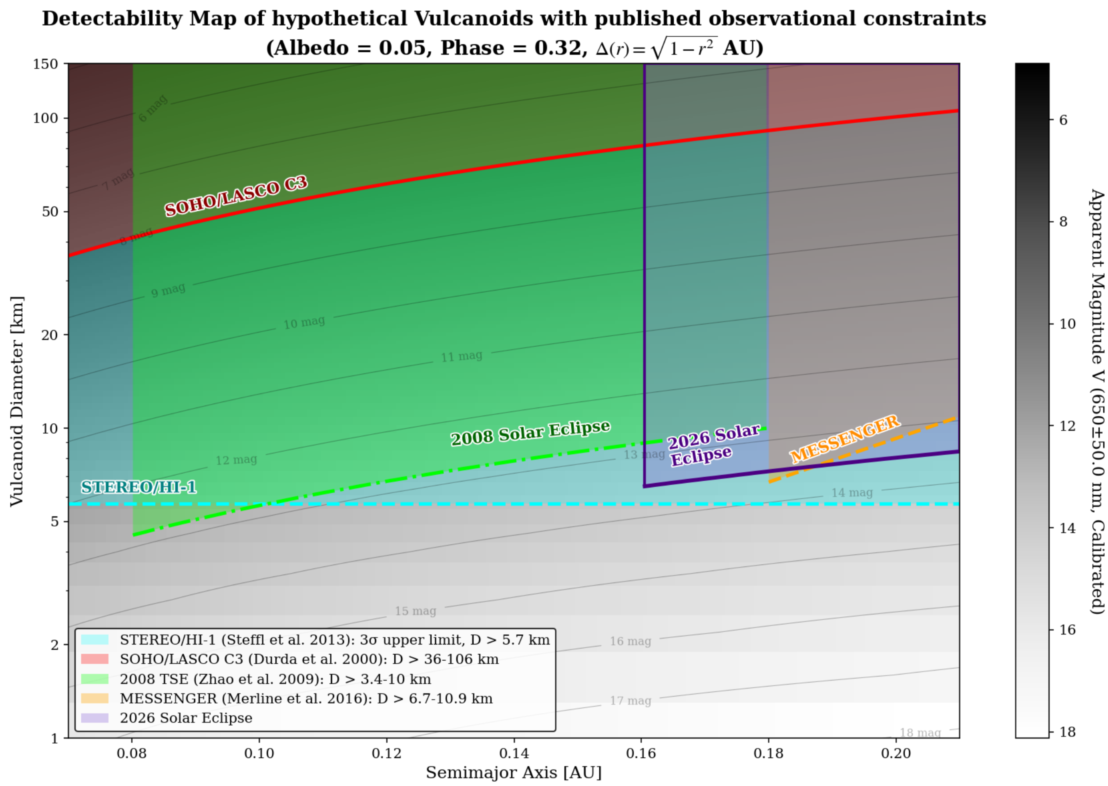

Figure 7.1: Detectability map of hypothetical Vulcanoids with published observational constraints. The background gradient and the corresponding black isolines indicate the apparent magnitude (V filter, 650 nm) predicted for bodies with a very dark albedo ($p_V = 0.05$) and a phase function similar to that of Mercury (evaluated at a solar phase angle of 90°, corresponding to greatest elongation). The brightness is calculated assuming observation at maximum solar elongation from an Earth-orbiting distance ($\Delta(r) = \sqrt{1-r^2}$ AU). The colored areas show the parameter space definitively excluded by the main search campaigns: the red curve denotes the limits of the SOHO/LASCO C3 coronagraph ($V < 8.0$); the green area illustrates the deep-magnitude limits ($V < 12.8$) reached during the 2008 total solar eclipse; the cyan area represents the stringent limits set by STEREO/HI-1: 3σ upper limit, diameter ($D > 5.7$ km); the orange region is the zone investigated directly in situ by the MESSENGER spacecraft ($0.18 - 0.21$ AU). Note that the MESSENGER limit (oblique line) does not follow the background isolines, as the observations were conducted from Mercury's orbit and not from the Earth. Finally, the purple region highlights the extended parameter space that will be targeted by our proposed solar eclipse campaigns, covering the outer Vulcanoid Zone from 0.16 to 0.21 AU down to a magnitude limit of $V = 13.5$.

by a horizontal line. Finally, the limits established by Merline et al. [57] form an oblique straight line. This geometry arises because the spacecraft MESSENGER conducted its search directly from Mercury's orbit, meaning that its observed target distance (Δ) was entirely different from that of an Earth-based observer, decoupling its limits from the background Earth-centric isolines. Constrained by thermal pointing limits, it only probed the outer region ($0.18 - 0.21$ AU) of the VZ, excluding dark bodies larger than $6.7 - 10.9$ km.

To provide a clear and comprehensive overview of the constraints imposed by these historical campaigns, the respective limiting magnitudes and the corresponding physical diameter limits-scaled to the uniform worst-case scenario of $p_V = 0.05$ are summarised in Table 7.1.

Table 7.1: Summary of the most significant historical Vulcanoid searches. For consistency with the detectability map (Figure 7.1), the original physical diameter limits have been scaled to represent the worst-case detection scenario, assuming a dark asteroid with geometric albedo $p_V = 0.05$ and a Mercury-like phase function. Asterisks (*) denote physical limits that vary dynamically depending on the heliocentric distance within the surveyed area.

Survey	**Year**	**Platform**	**Limiting Mag.**	**Diameter Limit**
Perrine & Campbell	1901–1909	Ground (Eclipse)	$8.0 - 9.0$	> 48 km
SOHO/LASCO C3	2000	Space	8.0	$36 - 106$ km*
Zhao et al.	2008	Ground (Eclipse)	12.8	$3.4 - 10$ km*
STEREO/HI-1	2013	Space	13.0	5.7 km
MESSENGER	2016	Space (Mercury orbit)	8.0	$6.7 - 10.9$ km*

From a dynamical perspective, collision and erosion rates decrease with increasing distance from the Sun. Therefore, the region with the highest probability of harbouring surviving objects of kilometre size is located at the outer edge of the stability zone, specifically between 0.16 and 0.18 AU [80] [39]. Evans and Tabachnik (2002) defined the precise geocentric ecliptic coordinates for this optimal search region, indicating that observations must focus on ecliptic longitudes of $9° \leq |l_g| \leq 10°$ and strictly narrow ecliptic latitudes of $|\beta_g| < 1°$ [39]. Finally, to overcome the Signal-to-Noise Ratio (SNR) limitations inherent to the visible spectrum, the optimal strategy is to target the mid-wave infrared (MWIR) band. If Vulcanoids exist, their equilibrium temperatures range between 700 and 850 K, placing their thermal emission peak directly within the 3 to 5 μm window [5]. Future campaigns must target this specific band by utilising platforms free from terrestrial atmospheric absorption, such as stratospheric telescopes or high-altitude aircraft. As demonstrated for solar astronomy by Caspi et al. [21], airborne platforms provide a definitive opportunity to detect this elusive primordial asteroid population.

Building on these theoretical and observational foundations, the second part of this thesis evaluated the practical feasibility of detecting the remaining kilometer-sized Vulcanoids during upcoming Total Solar Eclipses (TSEs). In parallel, a detailed climatological analysis was included to assess historical weather patterns, cloud coverage, and atmospheric conditions along the path of totality. Léon has been selected as the optimal site for the upcoming observational campaign during the August 2026 TSE. The primary objective of this mission is to rigorously test and validate the observational instrumentation under eclipse conditions, serving as a critical preparatory step for the

2027 eclipse. While the principal aim remains technical validation, this campaign also presents a tangible opportunity to achieve the first detection of a Vulcanoid.

Ultimately, this thesis aims to open a new active chapter in the search for this unexplored asteroid belt, bridging the gap between theoretical models and observational strategies.

Bibliography

[1] R. Almeida, C. A. Angeli, R. Duffard, and D. Lazzaro. Rotation periods for small main-belt asteroids. *Astronomy & Astrophysics*, 415:403–406, 2004.

[2] Jay Anderson. Total solar eclipse 2027 august 2, 2025.

[3] Jay Anderson. Total solar eclipse 2026 august 12. `https://eclipsophile.com/tse2026/`, 2026.

[4] R. Baum and W. Sheehan. *In Search of Planet Vulcan: The Ghost in Newton's Clockwork Universe.* Plenum Press, New York, 1997.

[5] Martin Beech and Lowell Peltier. The vulcanoid asteroids: Past, present and future. *American Journal of Astronomy and Astrophysics*, 5(3):28–41, 2017.

[6] Johann Elert Bode. *Anleitung zur Kenntniss des gestirnten Himmels.* Hamburg, 1772.

[7] Charles Bonnet. *Betrachtung über die Natur.* J. Friedrich Junius, Leipzig, 1766. German translation by J. D. Titius, including his insertion on the distances of the planets (the first formulation of the Titius-Bode law) on pp. 7-8 of the first part.

[8] William F. Jr. Bottke, Alessandro Morbidelli, Robert Jedicke, Jean-Marc Petit, Harold F. Levison, Patrick Michel, and Travis S. Metcalfe. Debiased orbital and absolute magnitude distribution of the near-earth objects. *Icarus*, 156:399–433, 2002.

[9] William F. Jr. Bottke, David Vokrouhlický, David P. Rubincam, and David Nesvorný. The yarkovsky and yorp effects: Implications for asteroid dynamics. *Annual Review of Earth and Planetary Sciences*, 34:157–191, 2006.

[10] A. Bouvier and M. Wadhwa. The age of the solar system redefined by the oldest pb–pb age of a meteoritic inclusion. *Nature Geoscience*, 3:637–641, 2010.

[11] Lis Brack-Bernsen and John M. Steele. Eclipse prediction and the length of the saros in babylonian astronomy. *Centaurus*, 47(3):181–206, 2005.

[12] Ernest W. Brown and Clarence A. Shook. *Planetary Theory.* At the University Press, 1933. Digitized by Osmania University.

[13] G. E. Brueckner et al. The large angle spectroscopic coronagraph (lasco). *Solar Physics*, 162(1-2):357–402, 1995.

[14] Schelte J. Bus and Richard P. Binzel. Phase ii of the small main-belt asteroid spectroscopic survey: A feature-based taxonomy. *Icarus*, 158(1):146–177, 2002.

[15] A. G. W. Cameron. The high density of mercury. Abstract presented at the Mercury Conference, August 1986.

[16] W. W. Campbell and R. Trumpler. Observations on the deflection of light in passing through the sun's gravitational field, made during the total solar eclipse of september 21, 1923. *Publications of the Astronomical Society of the Pacific*, 35:158–163, June 1923.

[17] William Wallace Campbell. Reports of observatories: Lick Observatory, University of California. *Publications of the Astronomical Society of the Pacific*, 21(128):213–223, 1909.

[18] H. Campins, D. R. Davis, S. J. Weidenschilling, and M. Magee. Searching for vulcanoids. In T. W. Rettig and J. M. Hahn, editors, *Completing the Inventory of the Solar System*, volume 107 of *Astronomical Society of the Pacific Conference Series*, pages 85–96, 1996.

[19] Albino Carbognani. *L'asteroide di Sodoma e Gomorra: Gli asteroidi e il rischio di collisione con la Terra – da Chicxulub ad Apophis senza dimenticare 'Oumuamua.* In Riga Edizioni, Italia, 2022.

[20] Albino Carbognani, Alberto Buzzoni, Manuel Barbetta, and Paolo Bacci. Photometric characterization of near-earth asteroids: rotation, taxonomy, and evidence for internal cohesion. *Preprint submitted to Elsevier*, 2026.

[21] Amir Caspi et al. A new facility for airborne solar astronomy: Nasa's wb-57 at the 2017 total solar eclipse. *The Astrophysical Journal*, 895:131, 2020.

[22] Henry Cavendish. Experiments to determine the density of the earth. *Philosophical Transactions of the Royal Society of London*, 88:469–526, 1798.

[23] Clark R. Chapman, David Morrison, and Ben Zellner. Surface properties of asteroids: A synthesis of polarimetry, radiometry, and spectrophotometry. *Icarus*, 25(1):104–130, 1975.

[24] Beth E. Clark, Bruce Hapke, Carle M. Pieters, and Daniel Britt. Asteroid space weathering and regolith evolution. In William F. Bottke, Alberto Cellino, Paolo Paolicchi, and Richard P. Binzel, editors, *Asteroids III*, pages 585–599. University of Arizona Press, Tucson, AZ, 2002.

[25] H. Courten. *Bulletin of the American Astronomical Society*, 8:504, 1976.

[26] Clifford Cunningham. The discovery of pallas. In *Early Investigations of Ceres and the Discovery of Pallas: Historical Studies in Asteroid Research*, pages 95–120. Springer, 2016.

[27] Clifford J. Cunningham. The discovery of vesta. In Clifford J. Cunningham, editor, *Investigating the Origin of the Asteroids and Early Findings on Vesta: Historical Studies in Asteroid Research*, pages 87–117. Springer, Cham, 2017.

[28] Gonzalo Carlos de Elía and Adrian Brunini. Collisional and dynamical evolution of the main belt and nea population. *Astronomy & Astrophysics*, 466(3):1159–1177, 2007.

[29] F. E. DeMeo, C. M. O'D. Alexander, K. J. Walsh, H. Busemann, and R. P. Binzel. The compositional structure of the asteroid belt. In P. Michel et al., editors, *Asteroids IV*, pages 13–41. University of Arizona Press, Tucson, 2015.

[30] Francesca E. DeMeo and Richard P. Binzel. An extension of the bus asteroid taxonomy into the near-infrared. *Icarus*, 202(1):160–180, 2009.

[31] D. Domingue, K. Lumme, J. Peltoniemi, and A.W. Harris. Application of photometric models to asteroids. In R.P. Binzel, T. Gehrels, and M.S. Matthews, editors, *Asteroids II*, pages 524–556. University of Arizona Press, 1989.

[32] Daniel D. Durda et al. A new observational search for vulcanoids in soho/lasco coronagraph images. *Icarus*, 148:312–315, 2000.

[33] J. Durech et al. Detection of the yorp effect in asteroid (1620) geographos. *Astronomy & Astrophysics*, 489:L25–L28, 2008.

[34] Noor e Aisha. The Mysterious Planet Vulcan: Myth, Discovery Claims, and Disproof Explained, 7 2025.

[35] Albert Einstein. Erklärung der perihelbewegung des merkur aus der allgemeinen relativitätstheorie. *Sitzungsberichte der Königlich Preußischen Akademie der Wissenschaften (Berlin)*, pages 831–839, 1915.

[36] Fred Espenak. Total solar eclipse of 2027 aug 02. `https://www.eclipsewise.com/solar/SEprime/2001-2100/SE2027Aug02Tprime.html`.

[37] Fred Espenak. Total solar eclipse of 2026 aug 12. `https://www.eclipsewise.com/solar/SEprime/2001-2100/SE2026Aug12Tprime.html`, 2022.

[38] Fred Espenak. Eclipses and the saros, n.d.

[39] N. W. Evans and S. A. Tabachnik. Structure of possible long-lived asteroid belts. *Monthly Notices of the Royal Astronomical Society*, 333:49–58, 2002.

[40] N. Wyn Evans and Serge Tabachnik. Possible long-lived asteroid belts in the inner solar system. *Nature*, 399:41–43, May 1999.

[41] C. J. Eyles et al. The heliospheric imagers onboard the stereo mission. *Solar Physics*, 254(2):387–445, 2009.

[42] Wesley C. Fraser, Michael E. Brown, Alessandro Morbidelli, Alex Parker, and Konstantin Batygin. The absolute magnitude distribution of kuiper belt objects. *The Astrophysical Journal*, 782(2):100, 2014.

[43] Gustav Adolph Goehner. Series of instantaneous telescopic views of the total eclipse [of the sun] July 29th, 1878. Miniature book, Library of Congress, Rare Book and Special Collections Division, 1878.

[44] J. Gradie and E. Tedesco. Compositional structure of the asteroid belt. *Science*, 216(4553):1405–1407, 1982.

[45] Alan W. Harris. On the revision of radiometric albedos and diameters of asteroids. *Icarus*, 126:450–454, 1997.

[46] Alan W. Harris and Giovanni D'Abramo. The population of near-earth asteroids. *Icarus*, 257:302–312, 2015.

[47] A.W. Harris and J.S.V. Lagerros. Asteroids in the thermal infrared. In W.F. Bottke, A. Cellino, P. Paolicchi, and R.P. Binzel, editors, *Asteroids III*, pages 205–218. University of Arizona Press, 2002.

[48] INAF. Comete e Asteroidi Near-Erth, 2025. `https://sorvegliatispaziali.inaf.it/comete-e-asteroidi-near-earth/`.

[49] B. Jenkins. Vulcan and bode's law. *Nature*, 19:74, 1878.

[50] Hiroshi Kimura and Ingrid Mann. Brightness of the solar f-corona. *Earth, Planets and Space*, 50(6):493–499, 1998.

[51] Daniel Kirkwood. On the distribution of the asteroids. *Proceedings of the American Philosophical Society*, 11:93–95, 1867.

[52] Gerard P. Kuiper. On the origin of the solar system. In J. A. Hynek, editor, *Astrophysics: A Topical Symposium*, pages 357–424. McGraw-Hill, New York, 1951.

[53] Martha A. Leake et al. The chronology of mercury's geological and geophysical evolution: The vulcanoid hypothesis. *Icarus*, 71(3):350–375, 1987.

[54] Renu Malhotra. The origin of Neptune's peculiar orbit. *Nature*, 376(6538):327–329, 1995.

[55] E. E. Mamajek, A. Prsa, G. Torres, P. Harmanec, M. Asplund, P. D. Bennett, N. Capitaine, J. Christensen-Dalsgaard, E. Depagne, W. M. Folkner, et al. IAU 2015 Resolution B3 on recommended nominal conversion constants for selected solar and planetary properties. *arXiv preprint arXiv:1510.07674*, 2015.

[56] Joseph Masiero, Robert Jedicke, Josef Durech, Stephen Gwyn, Larry Denneau, and Jeff Larsen. The thousand asteroid light curve survey. *Icarus*, 204:145–171, 2009.

[57] William J. Merline et al. Search for vulcanoids and mercury satellites from messenger. In *47th Lunar and Planetary Science Conference*, 2016.

[58] Andrea Milani, Steven R. Chesley, Maria Eugenia Sansaturio, Giacomo Tommei, and Giovanni B. Valsecchi. Nonlinear impact monitoring: Line of variation searches for impactors. *Icarus*, 173:362–384, 2005.

[59] Minor Planet Center. About the minor planet center. `https://minorplanetcenter.net/about`, 2025.

[60] A. Morbidelli, K. J. Walsh, D. P. O'Brien, D. A. Minton, and W. F. Bottke. The dynamical evolution of the asteroid belt. In P. Michel et al., editors, *Asteroids IV*, pages 493–507. University of Arizona Press, Tucson, 2015.

[61] Alessandro Morbidelli, Harold F. Levison, Kleomenis Tsiganis, and Rodney Gomes. Chaotic capture of jupiter's trojan asteroids in the early solar system. *Nature*, 435(7041):462–465, 2005.

[62] Alessandro Morbidelli, Kleomenis Tsiganis, Aurélien Crida, Harold F. Levison, and Rodney Gomes. Dynamics of the giant planets of the solar system in the gaseous protoplanetary disk and their relationship to the current orbital architecture. *The Astronomical Journal*, 134:1790–1798, 2007.

[63] Luca Nardi. *Pianeti mancanti. Da Plutone a Planet Nine, gli astri erranti nascosti nell'oscurità*. Edizioni Dedalo, 2025. Parte quarta.

[64] Near-Earth Object Science Definition Team. Update to determine the feasibility of enhancing the search and characterization of near-earth objects. Technical report, National Aeronautics and Space Administration, Washington, DC, September 2017. Prepared at the request of NASA Science Mission Directorate, Planetary Science Division.

[65] Michael M. Nieto. *The Titius-Bode Law of Planetary Distances: Its History and Theory*. Pergamon Press, Oxford, 1972.

[66] Ernst J. Öpik. Collision probabilities with the planets and the distribution of interplanetary matter. *Proceedings of the Royal Irish Academy. Section A: Mathematical and Physical Sciences*, 54:165–199, 1951.

[67] Lowell Francis Peltier. Vulcanoids: An examination of the intra-mercurial region. Master of science thesis, University of Regina, Regina, Saskatchewan, September 2019.

[68] D. Perna, M.A. Barucci, L. Drube, A. Falke, M. Fulchignoni, A.W. Harris, A.W. Harris, and Z. Kanuchova. A global response roadmap to the asteroid impact threat: The neoshield perspective. *Planetary and Space Science*, 118:311–317, 2015. SI:ACM Interrelated.

[69] C. D. Perrine. *Lick Observatory Bulletin*, 4:115, 1906.

[70] Charles D. Perrine. Results of the search for an intra-Mercurial planet in the total solar eclipse of 1901, May 18. *Lick Observatory Bulletin*, 1:183–187, 1902.

[71] Charles D. Perrine. The search for intramercurial bodies at the total solar eclipse of January 3, 1908. *Lick Observatory Bulletin*, 5(152):95–97, 1909.

[72] Andrej Prša, Petr Harmanec, Guillermo Torres, Eric Mamajek, Martin Asplund, Nicole Capitaine, Jørgen Christensen-Dalsgaard, Éric Depagne, Margit Haberreiter, Saskia Hekker, et al. Nominal values for selected solar and planetary quantities: Iau 2015 resolution b3. *The Astronomical Journal*, 152(2):41, 2016.

[73] H. P. Robertson. Dynamical effects of radiation in the solar system. *Monthly Notices of the Royal Astronomical Society*, 97:423–438, 1937.

[74] David P. Rubincam. Radiative spin-up and spin-down of small asteroids. *Icarus*, 148:2–11, 2000.

[75] David Parry Rubincam. Lageos orbit decay due to infrared radiation from earth. Technical Report NASA Technical Memorandum 87804, NASA Goddard Space Flight Center, Greenbelt, Maryland, USA, January 1987. Geodynamics Branch, Code 621.

[76] William Sheehan. James Craig Watson, First Director of Washburn Observatory: His Obsession with the Intra-Mercurial Planet Vulcan. *Bulletin of the American Astronomical Society*, 28:858, 1996.

[77] Thomas S. Statler. Extreme sensitivity of the yorp effect to small-scale topography. *Icarus*, 202(2):502–513, August 2009.

[78] A. J. Steffl et al. A search for vulcanoids with the stereo heliospheric imager. *Icarus*, 223:48–56, 2013.

[79] S. Alan Stern. Collisional time scales in the kuiper disk and their implications. *Astronomical Journal*, 110:856, August 1995.

[80] S. Alan Stern and Daniel D. Durda. Collisional evolution in the vulcanoid region: Implications for present-day population constraints. *Icarus*, 143:360–370, 2000.

[81] Lewis Swift. Discovery of Vulcan. *Nature*, 18(464):539–539, 1878.

[82] G. Jeffrey Taylor. Wandering gas giants and lunar bombardment. *Planetary Science Research Discoveries*, August 2006.

[83] David J. Tholen. *Asteroid taxonomy from cluster analysis of photometry*. PhD thesis, University of Arizona, Tucson, AZ, 1984.

[84] Chadwick A. Trujillo and Michael E. Brown. The radial distribution of the Kuiper belt. *The Astrophysical Journal*, 554(1):L95–L98, 2001.

[85] Fumihiko Usui, Toshihiro Kasuga, Sunao Hasegawa, Masateru Ishiguro, Daisuke Kuroda, Thomas G. Müller, Takafumi Ootsubo, and Hideo Matsuhara. Albedo properties of main belt asteroids based on the all-sky survey of the infrared astronomical satellite akari. *The Astrophysical Journal*, 762(1):56, 2013.

[86] D. Vokrouhlický, D. Nesvorný, M. Brož, W. F. Bottke, R. Deienno, C. D. Fuls, and F. C. Shelly. Orbital and absolute magnitude distribution of the hilda population. *Astronomical Journal*, 169(5):242, 2025.

[87] David Vokrouhlický. A complete linear model for the yarkovsky thermal force on spherical asteroid fragments. *Astronomy and Astrophysics*, 344:362–366, 1999.

[88] David Vokrouhlicky, William F. Bottke, Steven R. Chesley, Daniel J. Scheeres, and Thomas S. Statler. The yarkovsky and yorp effects. *arXiv:1502.01249 [astro-ph.EP]*, 2015. To appear in Space Science Series Book: Asteroids IV.

[89] David Vokrouhlický, Paolo Farinella, and William F. Bottke, Jr. The depletion of the putative vulcanoid population via the yarkovsky effect. *Icarus*, 148(1):147–152, 2000.

[90] Kevin J. Walsh, Alessandro Morbidelli, Sean N. Raymond, David P. O'Brien, and Avi M. Mandell. A low mass for mars from jupiter's early gas-driven migration. *Nature*, 475(7355):206–209, 2011.

[91] G. W. Wetherill. Mercury may be a collision fragment. Abstract presented at the Mercury Conference, August 1986.

[92] Stanley P. Wyatt and Fred L. Whipple. The poynting-robertson effect on meteor orbits. *The Astrophysical Journal*, 111:134–141, 1950.

[93] M. R. Zambri, Z. Z. Abidin, A. Hasan, Z. A. Ibrahim, and C. Y. Hwang. Decrease in sky brightness during the total solar eclipse of 2009 july 22. *Monthly Notices of the Royal Astronomical Society*, 431(4):3123–3126, 2013.

[94] Ben Zellner, David J. Tholen, and Edward F. Tedesco. The eight-color asteroid survey: Results for 589 minor planets. *Icarus*, 61(3):355–416, 1985.

[95] HaiBin Zhao et al. The search for vulcanoids in the 2008 total solar eclipse. *Science in China Series G: Physics, Mechanics & Astronomy*, 52(11):1790–1793, 2009.